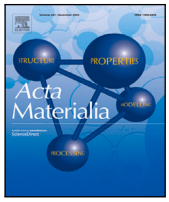
Acta Materialia 268 (2024) 119774



Contents lists available at ScienceDirect

Acta Materialia

journal homepage: www.elsevier.com/locate/actamat



Full length article

# Quantifying phase mixing and separation behaviors across length and time scales

M. Skolnick [a], S. Torquato [a,b,c,d,*]

[a] Department of Chemistry, Princeton University, Princeton, NJ, 08544, USA
[b] Department of Physics, Princeton University, Princeton, NJ, 08544, USA
[c] Princeton Institute of Materials, Princeton University, Princeton, NJ, 08544, USA
[d] Program in Applied and Computational Mathematics, Princeton University, Princeton, NJ, 08544, USA

ARTICLE INFO

*Keywords:*
Hyperuniformity
Mixing metric
Heterogeneous materials
Alloying
Blending

ABSTRACT

Phase mixing and separation phenomena abound in the formation of natural and synthetic material systems, including alloys, composites, granular media, geological media, complex fluids, and biological media. While characterizing phase mixing is critical to understanding material microstructure formation and physical properties, previous metrics that measure the degree of mixing in condensed phases often rely on empirical observation, are applicable only to certain microstructures, and/or fail to detect nontrivial changes in mixing with respect to length scale. To overcome these shortcomings, we introduce and study a mixing metric that is applicable to a broad spectrum of complex microstructures and leverages the hyperuniformity concept to provide a unifying framework to rank and classify mixing in materials across both length and time scales. Specifically, we employ the local phase volume-fraction/field-intensity variance $\sigma^2_{V/F}(R,t)$ associated with a spherical sampling window of radius $R$ at time $t$ as our metric. We demonstrate that $\sigma^2_{V/F}(R,t)$ provides a sensitive measure of mixing across both length and time scales of a structurally diverse set of real and simulated material microstructures: exotic disordered multihyperuniform avian retina photoreceptor cell patterns, time-evolving spinodal decomposition patterns, and a model material mixed via the baker's transformation. We also describe how this metric can be used to guide future work on fabricating materials whose bulk properties can be controlled by tuning their mixing characteristics across length and time scales.

## 1. Introduction

Spatial patterns are ubiquitous in materials science, where fundamental building blocks like atoms, molecules, nanoparticles, macromolecules, and grains form intricate structures in natural and synthetic situations [1–13] whose characteristic length and time scales range from nano- to macro-scale. A critically important characteristic of a broad spectrum of such spatial patterns is how well spatially mixed (or blended), alloyed, or homogeneous they are. A capacity to systematically rank, compare, and contrast these material structures according to their degree of mixing across length and time scales can help elucidate the physical forces driving their formation and time evolution [3,4,11,14–17] as well as their effective physical properties [5–7,18–25]. However, the tremendous diversity of geometrical structures spanning the order–disorder spectrum exhibited by these spatial patterns [4,5,13,26–28] at both different length and time scales presents great challenges to achieve such a mixture classification scheme. Fig. 1 provides illustrative examples of such diverse microstructures, including a model ordered-checkerboard composite microstructure [5] in Fig. 1(a), a phase-separated microstructure in Fig. 1(b), and a portion of the cosmic microwave background intensity [29], a well-known random scalar field, in Fig. 1(c).

To overcome these challenges, we propose a new mixing metric $\sigma^2_{V/F}(R,t)$, which measures local fluctuations in a system's phase volume-fraction/concentration field-intensity associated with a spherical sampling window of radius $R$ at time $t$ (see Section 2 for specific details) – generalizing previous work using the quantities $\sigma^2_V(R)$ [30–33] and $\sigma^2_F(R)$ [34,35] for characterizing time-independent microstructures. To get a sense of the diversity of microstructures that our mixing metric can characterize, we show in Fig. 1 three different two-dimensional images (ordered two-phase medium, phase-separated system, and a random scalar field) and corresponding sampling windows of radius $R$ for the local variance. By measuring the degree of mixing via compositional fluctuations, a unifying property of all spatial

* Corresponding author at: Department of Chemistry, Princeton University, Princeton, NJ, 08544, USA.
*E-mail address:* torquato@electron.princeton.edu (S. Torquato).

[1] By definition, Danckwerts' "scale of segregation" metric $S$ only provides an estimate of phase aggregate size [1], a relatively short-range property.

https://doi.org/10.1016/j.actamat.2024.119774
Received 20 December 2023; Received in revised form 14 February 2024; Accepted 16 February 2024
Available online 17 February 2024
1359-6454/© 2024 Acta Materialia Inc. Published by Elsevier Ltd. All rights reserved.




**Fig. 1.** Sampling windows of radius $R$ for the local variance (yellow shaded circles) for three different two-dimensional systems that represent the diversity of spatial patterns with distinct phase mixing and separation characteristics: (a) an ordered checkerboard composite microstructure, (b) a phase-separated microstructure, and (c) a portion of the cosmic microwave background intensity [43], which is a prototypical example of a random scalar field. In (a) and (b), the two discrete phases are colored in red and blue. In (c), blue and red correspond to regions of low and high temperature, respectively. (For interpretation of the references to color in this figure legend, the reader is referred to the web version of this article.)
*Source:* This figure is adapted from Ref. [40].

patterns, across space and time, our mixing metric can be applied to a wide-variety of complex microstructures — setting it apart from existing mixing metrics which are typically limited to time-dependent and time-independent microstructures that consist of discrete particles [19,36–38]. While well-known mixing metrics like Danckwerts' "intensity of segregation metric" $I$ [1] or Lacey's "mixing index" $M$ [39] are applicable to more general time-dependent and time-independent spatial patterns, they only measure mixing at individual points in the system. As such, these previously proposed metrics are insensitive to important length scale-dependent variations in mixing behavior.[1]

In contrast, our metric $\sigma^2_{V/F}(R,t)$ explicitly incorporates non-trivial [40] information about mixing related to spatial correlations via the sampling window radius $R$. We note that while the mixing metrics based on the Rényi statistical entropy introduced in Refs. [41,42] are functions of both length and time and certainly improvements over the metrics $I$ and $M$, they have difficulty distinguishing mixing in microstructures at large-length scales. Additionally, the rankings of mixing in systems by such metrics are input parameter-dependent. Our metric, on the other hand, does not require input parameters and is sensitive to variations in mixing across all length and time scales (see Section 2.2 for details).

The importance of characterizing disordered spatial patterns at various length scales has become increasingly apparent in recent years with the analysis of the local variance $\sigma^2(R)$ associated with a spherical window of radius $R$ and the discovery of exotic disordered hyperuniform point patterns [44]. The hyperuniformity concept was then subsequently generalized to treat two-phase heterogeneous media [33] as well as scalar and vector fields [34]. In all cases, disordered hyperuniform materials possess a hidden form of long-range order in which the material is globally uniform, despite not being crystalline [40]. Since they are characterized by an anomalous suppression of density or volume-fraction fluctuations relative to garden-variety disordered non-hyperuniform materials [33,40,44], disordered hyperuniform materials are receiving considerable attention [16,45–66].

As a state of matter that lies between a crystal and a typical liquid, disordered hyperuniform materials can be endowed with novel directionally independent physical properties that are robust with respect to defects [40]. Examples of such materials include avian retina photoreceptor patterns [46], photonic and phononic band gap materials [67–71], multifunctional materials [23,72–75], special optical and lasing materials [76–81], certain medium entropy alloys [61], transparent materials [23,48,50,73,74,82–84], materials endowed with optimal transport [85,86] and mechanical properties [87], as well as conductive disordered two-dimensional materials [60,88]. The reader is referred to Refs. [40,75] for comprehensive reviews on hyperuniformity and hyperuniform materials.

Hyperuniformity provides a unifying framework for classifying materials according to their anomalous suppression of density fluctuations at large length scales. Such long-range density fluctuations in a material can be measured via the time-independent local volume-fraction/scalar field-intensity variance $\sigma^2_{V/F}(R)$ associated with a spherical sampling window of radius $R$ (depicted schematically in Fig. 1) in the large-$R$ asymptotic limit [30,33,34,40]. Naturally, this long-distance regime of $\sigma^2_V(R)$ is central to the hyperuniformity concept (see Section 2.2 for specific details). In our recent work [28], we further extended the utility of $\sigma^2_V(R)$ as a microstructural probe by demonstrating its utility as a robust metric of order/disorder at *any* length scale $R$ in heterogeneous materials. We specifically found that greater disorder (order) across a length scale $R$ results in a (larger) smaller value of $\sigma^2_V(R)$.

In this work, we extend the local volume-fraction/field-intensity variance $\sigma^2_{V/F}(R)$ to also include time dependence, i.e., $\sigma^2_{V/F}(R,t)$, thus providing a unified and rigorous means to systematically rank and classify phase mixing and separation across length $R$ and time $t$ scales in spatial patterns consisting of discrete phases or concentration fields. Additionally, we define a $3\times 3$ "mixing matrix" $\mathcal{M}$ in which the entries are values of $\sigma^2_{V/F}(R,t)$ evaluated at all 9 combinations of system-specific, selected small-, intermediate-, and large-length (i.e., $R_{s/i/l}$) and time (i.e., $t_{s/i/l}$) scales (see Sections 4 and 5 for additional details). We show how the matrix $\mathcal{M}$ can be used to quantitatively extract overall mixing trends across both length and time scales as a supplement to the detailed information contained in $\sigma^2_{V/F}(R,t)$. To demonstrate the utility of the mixing metric $\sigma^2_{V/F}(R,t)$ and matrix $\mathcal{M}$, we test them on a diverse set of real and simulated material microstructures with distinct phase geometries with varying degrees of order/disorder. We also discuss ways that $\sigma^2_{V/F}(R,t)$ and $\mathcal{M}$ can be used in combination to guide the inverse design of materials with desirable effective physical properties by tuning their mixing characteristics across both length and time scales. While our focus in this paper is on the quantification of mixing in materials, we note that our metric is readily applied to spatial patterns arising in other fields including physics [89], biology [90], ecology [91], and mathematics [92].

As a first test of our metric, we examine the mixing characteristics of experimentally obtained time-independent avian retina photoreceptor patterns consisting of five different types of cone cells [26,46]. We specifically quantify mixing in this system via the metric $\sigma^2_V(R)$ and demonstrate how disordered hyperuniform mixtures can exhibit a

greater degree of mixing than disordered nonhyperuniform ones above certain length scales (see Section 5.1 for more information). The metric also shows how the mixing in this system is destroyed by certain random perturbations.

As a second test our metric, we bring in the additional complexity of time by examining the well-known time-evolving spinodal decomposition pattern, which we simulate via the Cahn-Hilliard equation [93,94]. This system is a natural example to explore the time-dependent transition of a nonhyperuniform mixture to a hyperuniform one [35,95], which we study using the metric $\sigma_F^2(R,t)$. We find that this transition is characterized by a gradual increase in mixing at large length scales over time until the system attains hyperuniformity (see Section 5.2 for details). Our metric also reveals the existence of a structurally distinct, transient hyperuniform state at intermediate-times prior to the emergence of the so-called "scaling regime" pattern which is also hyperuniform [35].

As a final test of the sensitivity of our mixing metric, we devise a new two-phase model microstructure that undergoes an order–disorder transition by repeated application of the baker's map. Originally a purely mathematical transformation [96], the baker's map has been applied in simulated and experimental systems by the fluids and polymers communities [21,22,97–100]. In short, our two-phase model mixture evolves over time from a hyperuniform and phase-separated state to a disordered, isotropic and nonhyperuniform mixed one (see Section 5.3 for specific details). We examine the length- and time-dependent mixing behaviors of this system using our metric and the mixing matrix $\mathcal{M}$, which reveal that the dynamical destruction of hyperuniformity in this system is characterized by a sequential erosion of order over increasingly smaller length scales until the system cannot be mixed any further. Through theory and simulation, we show that such "mixing invariant" structures occur after a "characteristic mixing time" $\tau_M$ that grows logarithimically with the system size (see Section 5.4 for details). We supplement our analysis of this disorder-order transition with the first determination of the spectral density (i.e., scattering) data for a heterogeneous microstructure evolving under the baker's transformation.

In Section 2, we provide basic definitions and key background material. Section 3 describes the microstructures that we examine. The mixing matrix $\mathcal{M}$ is introduced in Section 4. The main results of the paper are presented in Section 5. Conclusions and future research directions are discussed in Section 6.

## 2. Definitions and background

In this section, we introduce key concepts and definitions used to describe multi-phase microstructures and scalar fields; including correlation functions, and the classification of hyperuniform and nonhyperuniform materials.

### 2.1. Correlation functions

The microstructure of a multi-phase material with $P$ phases in $d$-dimensional Euclidean space $\mathbb{R}^d$ at time $t$ is uniquely determined by the indicator functions $\mathcal{I}^{(i)}(\mathbf{x},t)$ for the individual discrete phases which are defined as

$$\mathcal{I}^{(i)}(\mathbf{x},t) = \begin{cases} 1, & \mathbf{x} \text{ in phase } i \text{ at time } t \\ 0, & \mathbf{x} \text{ otherwise} \end{cases}, \tag{1}$$

where $i = 1,\dots,P$ and $\mathbf{x}$ is a position vector [5,101]. The $n$-point correlation function $S_n^{(i)}$ for phase $i$ is defined as [5]

$$S_n^{(i)}(\mathbf{x}_1,\mathbf{x}_2,\dots,\mathbf{x}_n,t) = \left\langle \prod_{j=1}^{n} \mathcal{I}^{(i)}(\mathbf{x}_j,t) \right\rangle \tag{2}$$

where the angular brackets denote an ensemble average. The quantity $S_n^{(i)}(\mathbf{x}_1,\mathbf{x}_2,\dots,\mathbf{x}_n,t)$ can be interpreted as the probability of finding the ends of all vectors $\mathbf{x}_1,\dots,\mathbf{x}_n$ in phase $i$ at time $t$. Using the expression (2), we can write the one-point correlation function as [5]

$$S_1^{(i)}(t) = \langle \mathcal{I}^{(i)}(\mathbf{x},t) \rangle \tag{3}$$

which is equal to the volume fraction of phase $i$ at time $t$, $\phi_i(t)$. Similarly, the two-point correlation function is written as

$$S_2^{(i)}(\mathbf{x}_1,\mathbf{x}_2,t) = \langle \mathcal{I}^{(i)}(\mathbf{x}_1,t)\mathcal{I}^{(i)}(\mathbf{x}_2,t) \rangle. \tag{4}$$

For statistically homogeneous multi-phase materials in which there are no preferred centers, this quantity only depends on the relative displacement vector $\mathbf{r} = \mathbf{x}_2 - \mathbf{x}_1$ and thus $S_2^{(i)}(\mathbf{x}_1,\mathbf{x}_2,t) = S_2^{(i)}(\mathbf{r},t)$ [5]. Then, the time-dependent autocovariance function is given by [5]

$$\chi_V(\mathbf{r},t) \equiv S_2^{(i)}(\mathbf{r},t) - \phi_i^2(t). \tag{5}$$

For statistically isotropic materials, the autocovariance function depends only on the magnitude $r = |\mathbf{r}|$ of the displacement vector. We define the time-dependent spectral density $\tilde{\chi}_V(\mathbf{k},t)$ as the Fourier transform of $\chi_V(\mathbf{r},t)$ at wavevector $\mathbf{k}$, i.e.,

$$\tilde{\chi}_V(\mathbf{k},t) = \frac{1}{(2\pi)^d} \int_{\mathbb{R}^d} \chi_V(\mathbf{r},t) e^{i\mathbf{k}\cdot\mathbf{r}} d\mathbf{r}. \tag{6}$$

One can measure the spectral density, which is a non-negative real-valued function of $\mathbf{k}$, directly in the laboratory via elastic scattering experiments [102].

In what follows, we show that the time-dependent local volume-fraction variance $\sigma_V^2(R,t)$ (i.e., the mixing metric for multi-phase materials) can be expressed by the following equivalent real- and Fourier-space integrals, which notationally are trivial extensions of the time-independent counterparts [30,33,34]:

$$\begin{aligned} \sigma_V^2(R,t) &= \frac{1}{v_1(R)} \int_{\mathbb{R}^d} \chi_V(\mathbf{r},t)\alpha_2(r;R)d\mathbf{r} \\ &= \frac{1}{v_1(R)(2\pi)^d} \int_{\mathbb{R}^d} \tilde{\chi}_V(\mathbf{k},t)\tilde{\alpha}_2(k;R)d\mathbf{k}. \end{aligned} \tag{7}$$

In these expressions, $\alpha_2(r;R)$ is the scaled intersection volume of two spherical windows of radius $R$ separated by a distance $r$ (know analytically in any dimension [103]), $v_1(R)$ is the observation window volume, and $\tilde{\alpha}(k;R)$ is the Fourier transform of $\alpha_2(r;R)$ which is given exactly by the expression [34]

$$\tilde{\alpha}(k;R) = 2^d \pi^{d/2} \Gamma(d/2+1) \frac{[J_{d/2}(kR)]^2}{k^d}, \tag{8}$$

where $\Gamma(x)$ is the Gamma function. We use spherical observation windows in this paper, so the $d$-dimensional window volume is $v_1(R) = \pi^{d/2}R^d/\Gamma(d/2+1)$. We also note that $\sigma_V^2(R=0,t) = \phi_i(t)(1-\phi_i(t))$ [30], which sets an upper bound on the metric for multi-phase materials, i.e., $\sigma_V^2(R,t) \le \phi_i(t)(1-\phi_i(t))$ for all $R$ and $t$.

For scalar fields, we replace the time-dependent phase indicator function $\mathcal{I}^{(i)}(\mathbf{x},t)$ with the analogous real valued field-intensity function $F(\mathbf{x},t)$ in $\mathbb{R}^d$ [34]. The scalar field $F(\mathbf{x},t)$ could represent a time-varying concentration field [35] and can be interpreted as a multi-phase microstructure in which there is an infinite number of phases. The autocovariance function for $F(\mathbf{x},t)$ is [34]

$$\psi(\mathbf{r},t) = \langle [F(\mathbf{x}_1,t) - \langle F(\mathbf{x}_1,t)\rangle][F(\mathbf{x}_2,t) - \langle F(\mathbf{x}_2,t)\rangle] \rangle. \tag{9}$$

The corresponding non-negative and real-valued field spectral density is obtained via the Fourier transform [34]

$$\tilde{\psi}(\mathbf{k},t) = \int_{\mathbb{R}^d} \psi(\mathbf{r},t) e^{i\mathbf{k}\cdot\mathbf{r}} d\mathbf{r}. \tag{10}$$

Expressions for the time-dependent local field-intensity variance $\sigma_F^2(R,t)$ (i.e., the mixing metric for scalar fields) are similar to those [cf. Eq. (7)] used for $\sigma_V^2(R,t)$ [34]:

$$\sigma_F^2(R,t) = \frac{1}{v_1(R)} \int_{\mathbb{R}^d} \psi(\mathbf{r},t)\alpha_2(r;R)d\mathbf{r}$$

$$= \frac{1}{v_1(R)(2\pi)^d}\int_{\mathbb{R}^d}\tilde{\psi}(\mathbf{k},t)\tilde{\alpha}_2(k;R)d\mathbf{k}. \tag{11}$$

Lastly, note that $\sigma_F^2(R=0,t) = \langle F(\mathbf{x},t)\rangle(1-\langle F(\mathbf{x},t)\rangle)$ [34], which sets an upper bound on the metric for scalar fields, i.e., $\sigma_F^2(R,t) \leq \langle F(\mathbf{x},t)\rangle(1-\langle F(\mathbf{x},t)\rangle)$ for all $R$ and $t$.

### 2.2. Classification of hyperuniform and nonhyperuniform materials

We will assume statistically homogeneous multi-phase microstructures and fields in $d$-dimensional space at time $t$ whose spectral densities exhibit the following respective power-law forms:

$$\tilde{\chi}_V(\mathbf{k},t) \sim B(t)|\mathbf{k}|^{\alpha(t)}, \tag{12}$$

and

$$\tilde{\psi}(\mathbf{k},t) \sim C(t)|\mathbf{k}|^{\alpha(t)}, \tag{13}$$

where the exponent $\alpha(t)$ and coefficients $B(t)$ and $C(t)$ are now generally dependent on time. The hyperuniformity of time-varying multi-phase systems is defined by the following infinite-wavelength condition on the spectral density [33,34]:

$$\lim_{|\mathbf{k}|\to 0}\tilde{\chi}_V(\mathbf{k},t) = 0. \tag{14}$$

The analogous condition for time-varying hyperuniform scalar fields is given by the following limit of the field spectral density [34]:

$$\lim_{|\mathbf{k}|\to 0}\tilde{\psi}(\mathbf{k},t) = 0. \tag{15}$$

Equivalently, one can define hyperuniformity based on the local volume-fraction/field-intensity variance $\sigma_{V/F}^2(R,t)$ [28,33,34,40]. Specifically, a multi-phase material or concentration field is hyperuniform at time $t$ if the inverse of its variance grows in the large-$R$ limit *faster* than the observation window volume (i.e., $R^d$). This behavior contrasts that of typical disordered systems for which $\sigma_{V/F}^2(R,t)$ decays *as* the inverse of the spherical observation window volume.

Through the hyperuniformity concept, one can classify equilibrium and non-equilibrium states of matter, hyperuniform or not, according to their large-scale spatial fluctuations. For statistically homogeneous hyperuniform systems [33,40], there are three different classes (scaling regimes) that describe the associated large-$R$ behaviors of $\sigma_{V/F}^2(R,t)$ when the (field) spectral density goes to zero as a power-law scaling (i.e., Eqs. (12) or (13)) in the limit $|\mathbf{k}| \to 0$ [40]:

$$\sigma_{V/F}^2(R,t) \sim \begin{cases} R^{-(d+1)}, & \alpha(t) > 1 \quad \text{(Class I)} \\ R^{-(d+1)}\ln R, & \alpha(t) = 1 \quad \text{(Class II)} \\ R^{-(d+\alpha(t))}, & 0 < \alpha(t) < 1 \quad \text{(Class III).} \end{cases} \tag{16}$$

Classes I and III are the strongest and weakest forms of hyperuniformity, respectively. Class I systems include all perfect crystals, many quasicrystals and exotic disordered materials [40,75] and fields [35, 104]. An example of a crystalline class I hyperuniform two-phase microstructure is shown in Fig. 1(a). Also belonging to class I are stealthy hyperuniform systems which are defined to be those which exhibit zero-scattering intensity for a set of wave vectors around the origin [104], i.e., stealthy multi-phase materials have [34]

$$\tilde{\chi}_V(\mathbf{k},t) = 0 \qquad \text{for} \quad 0 \leq |\mathbf{k}| \leq K, \tag{17}$$

and stealthy scalar fields have [34]

$$\tilde{\psi}(\mathbf{k},t) = 0 \qquad \text{for} \quad 0 \leq |\mathbf{k}| \leq K. \tag{18}$$

Examples of stealthy multi-phase heterogeneous materials are periodic packings of spheres, disordered sphere packings derived from stealthy point patterns, as well as specially designed stealthy hyperuniform dispersions and medium-entropy alloys [61,85,86,104]. Stealthy hyperuniform scalar fields were first characterized in Ref. [35] and have been observed experimentally in certain amorphous laser-speckle patterns [105]. Multi-phase materials may also exhibit multihyperunifom order. In these systems, each phase is individually hyperuniform. This behavior has been previously observed in real [46] and simulated [61, 106] point patterns.

Any statistically homogeneous nonhyperuniform multi-phase material has a local variance with the following large-$R$ scaling behaviors [107]:

$$\sigma_V^2(R,t) \sim \begin{cases} R^{-d}, & \alpha(t) = 0 \quad \text{(typical nonhyperuniform)} \\ R^{-(d+\alpha(t))}, & -d < \alpha(t) < 0 \quad \text{(antihyperuniform).} \end{cases} \tag{19}$$

For statistically homogeneous scalar fields, the local field-intensity variance has identical large-$R$ scaling behaviors, i.e.,

$$\sigma_F^2(R,t) \sim \begin{cases} R^{-d}, & \alpha(t) = 0 \quad \text{(typical nonhyperuniform)} \\ R^{-(d+\alpha(t))}, & -d < \alpha(t) < 0 \quad \text{(antihyperuniform).} \end{cases} \tag{20}$$

A typical nonhyperuniform system has $\tilde{\chi}_V(0,t), \tilde{\psi}(0,t) > 0$ as can be seen via the power-laws (12) and (13), implying that $B(t) = \tilde{\chi}_V(0,t)$ and $C(t) = \tilde{\psi}(0,t)$. The spectral density of antihyperuniform systems is unbounded at the origin [107], i.e., antihyperuniform multi-phase materials and scalar fields have $\lim_{|\mathbf{k}|\to 0}\tilde{\chi}_V(\mathbf{k},t) \to +\infty$ and $\lim_{|\mathbf{k}|\to 0}\tilde{\psi}(\mathbf{k},t) \to +\infty$, respectively. These zero-wavevector conditions make antihyperuniform systems diametrically opposed to hyperuniform ones. Examples of antihyperuniform systems include systems at thermal critical points (e.g., liquid-vapor and magnetic critical points) [108, 109], fractals [110], disordered nonfractals [111], and certain substitution tilings [112]. An example image of an antihyperuniform two-phase microstructure is shown in Fig. 1(b).

A system is deemed "effectively hyperuniform" (i.e., hyperuniform for all intents and purposes) depending on the magnitude of its hyperuniformity index $H$, which is defined for multi-phase microstructures and scalar fields as [113],

$$H(t) \equiv \frac{\tilde{\chi}_V(0^+,t)}{\tilde{\chi}_V(k_{peak},t)} \tag{21}$$

and

$$H(t) \equiv \frac{\tilde{\psi}(0^+,t)}{\tilde{\psi}(k_{peak},t)}, \tag{22}$$

respectively. Here, $k_{peak}$ is the wavenumber corresponding to the largest peak in the spectral density. The condition for effective hyperuniformity in multi-phase systems and scalar fields is $H \leq 10^{-3}$ [35, 114]. We note that Eqs. (21) and (22) are exact in the infinite-system limit.

## 3. Microstructures

In this subsection, we summarize the salient details of the microstructures that we examine using the metric $\sigma_{V/F}^2(R,t)$. While we only examine systems in two-dimensional (2D) Euclidean space $\mathbb{R}^2$ in this paper, our methods are readily applied to general $d$-dimensional systems.

### 3.1. Avian retina photoreceptor patterns

Light sampling is essential for living organisms to interact with their surrounding environment. While the optimal sampling of light requires ordered arrangements of photoreceptor units [115], birds, which are known for their acute sense of vision, have disordered photoreceptor mosaics. As it turns out, the exquisite light sampling qualities of the avian retina are attributable to the exotic disordered *multihyperuniform* arrangement of the five types of photoreceptor cells (cones) within it [46], i.e., each cone population is individually hyperuniform in addition to the collective arrangement of cells also being hyperuniform. In short, multihyperuniform disorder balances the need for uniform light sampling by each cone type with their various packing constraints. The lack of crystallization in this system is attributed to the geometric frustration due to size and composition disparities of

the four single cone (violet, blue, green, and red) and one double cone species [46]. Furthermore, a statistical–mechanical formulation presented in Ref. [46] has modeled the multihyperuniform disorder in these photoreceptor patterns as a five-component system involving short-ranged hard-core repulsions between all cells and longer-ranged soft-repulsive interactions between pairs of like-cells.

### 3.2. Spinodal decomposition patterns

The Cahn-Hilliard equation [93,94] has been used to model phase-separation dynamics by spinodal decomposition in a multitude of natural and synthetic materials such as alloys [116], polymer blends [117], and biological fluids [13]. Additionally, spinodal phase decomposition has been exploited to manufacture porous materials with desirable mechanical properties [118–121] that can be tuned by varying their degrees of anisotropy and phase separation [122]. Here, we specifically simulate spinodal decomposition in 2D by evolving the concentration field $c \equiv c(\mathbf{x}, t)$ by the equation

$$\frac{\partial c}{\partial t} = \nabla \cdot (D \nabla \mu). \tag{23}$$

Here, $D$ is the diffusion coefficient and $\mu$ is the chemical potential which is a function of $c(\mathbf{x}, t)$ and the free energy density $f(c)$, and is defined as

$$\mu = f'(c) - \gamma \nabla^2 c. \tag{24}$$

The square-root of the parameter $\gamma$ sets the width of the transition regions between different phases. Following Ref. [35], we use the double-well form $f(c) = (c^2 - 1)^2/4$ for the free energy density. At long times, the system enters the so-called self-similar "scaling regime" in which the average domain size will continuously follow a $t^{1/3}$ power law while the system looks statistically the same [95]. We note that Ma and Torquato previously determined via simulations that such "scaling regime" patterns in 2D are class I hyperuniform with exponent $\alpha = 4$ [35].

### 3.3. The Baker's transformation

The baker's transformation (or map) is a nearly century-old concept from dynamical systems theory [96], that has been applied and studied as a mixing procedure by the fluids community [97–100]. Recently, the baker's transformation has been employed in the laboratory to efficiently manufacture polymer-nanoparticle composites [21] and polymer-based dielectric materials [22] with desirable physical properties that can be tuned by varying the number of transformation steps. It is named after the kneading procedure applied to dough by bakers: the dough is cut in half, the halves are stacked, compressed, and then the process repeats. In the context of material mixing, the "dough" is initially two stacked layers of the different materials to be mixed. Repeated application of the baker's transformation to the "dough" will result in a well-mixed microstructure consisting of many thin alternating layers of the two materials.

As an illustrative quantitative example, we can consider how an initial two-dimensional distribution of $N$ points in an $L \times L$ square evolves under the baker's transformation. A point $(x, y)$ in the initial configuration is labeled as species 1 (red) if $0 \le y < L/2$ or species 2 (blue) if $L/2 \le y < L$. The locations of all points are transformed via the baker's map as [96],

$$S_B(x, y) = \begin{cases} \left(2x, \frac{y}{2}\right), & 0 \le x < \frac{L}{2} \\ \left(2L - 2x, L - \frac{y}{2}\right), & \frac{L}{2} \le x < L. \end{cases} \tag{25}$$

To create a platform for examining time-dependent changes in mixing with the metric $\sigma^2_{V/F}(R, t)$, we have devised a new two-phase model microstructure that undergoes an order–disorder transition upon repeated application of the baker's map. The specific implementation details for this model are detailed in Section 5.3.

## 4. The mixing matrix $\mathcal{M}$

The metric $\sigma^2_{V/F}(R, t)$ provides a numerical score of mixing quality for any *specific point* in the ($R$-$t$) plane. To quantitatively extract overall mixing trends across all length and time scales as a supplement to the detailed information contained in $\sigma^2_{V/F}(R, t)$, we identify specific sampling window radii $R_s$, $R_i$, and $R_l$ that represent the overall mixing quality of the system's characteristic small-, intermediate-, and large-length scales. Analogously, we select specific times $t_s$, $t_i$, and $t_l$ that capture the overall mixing quality of the system's characteristic short-, intermediate-, and long-time scales. With these parameters, we can define the following "mixing matrix":

$$\mathcal{M} = \begin{bmatrix} \sigma^2_{V/F}(R_s, t_s) & \sigma^2_{V/F}(R_i, t_s) & \sigma^2_{V/F}(R_l, t_s) \\ \sigma^2_{V/F}(R_s, t_i) & \sigma^2_{V/F}(R_i, t_i) & \sigma^2_{V/F}(R_l, t_i) \\ \sigma^2_{V/F}(R_s, t_l) & \sigma^2_{V/F}(R_i, t_l) & \sigma^2_{V/F}(R_l, t_l). \end{bmatrix} \tag{26}$$

In addition to being specific sampling points, the values of $R_{s/i/l}$ and $t_{s/i/l}$ could also represent boundaries between regions of interest in the ($R$-$t$) plane. In such cases, the entries of the matrix $\mathcal{M}$ could be taken to be averages of the metric over those regions. In general, the precise selection of values for these characteristic length and time scales is application-dependent.

Specific choices for the parameters $R_{s/i/l}$ and $t_{s/i/l}$ for the microstructures considered in this paper are detailed in Sections 5.1–5.3. Corresponding numerical results for the matrix $\mathcal{M}$ are presented in these sections as well.

## 5. Results

### 5.1. Avian retina photoreceptor patterns

In this subsection, we present numerical results for the mixing metric $\sigma^2_V(R)$ for the static multihyperuniform avian photoreceptor patterns that were described in Section 3.1. We specifically examine multi-phase microstructures made by taking two-dimensional point patterns formed by the cell centroids that were obtained via fluorescence microscopy methods in a published study [26], and decorating each point with a nonoverlapping disk. In the absence of size-polydispersity information for these systems, we set each disk radius $a = 0.51$ micrometers, as this value is half of the smallest inter-particle distance among all of the configurations.[2] To study the sensitivity of multihyperuniform mixing to structural perturbations, we modify the photoreceptor arrangements in two different manners: randomly shuffling the identities (colors) of the photoreceptor cells, and equilibrating the system via Monte Carlo translational moves subject to the hard-disk non-overlapping constraint [10,123]. Representative images of the unperturbed, shuffled, and equilibrated configurations are shown in Figs. 2(a), 2(b), and 2(c), respectively.

To account for the lack of periodic boundaries in these experimental systems, we sample $\sigma^2_V(R)$ directly from the configurations using Monte Carlo methods. In doing so, we can explicitly avoid placing sampling windows of any size that would overlap with a configuration's boundaries. The 14 experimentally-obtained, multihyperuniform photoreceptor patterns consist of, on average, $N \sim 4400$ points (cells) total (see Refs. [26,46] for additional details). Here, we use the disk radius $a$ as the characteristic length scale for these systems. From each of the 14 multihyperuniform patterns, we generated 20 configurations each of the perturbed shuffled and equilibrated systems.

It is seen that all individual cell types in the unperturbed configurations are more well-mixed than those in the shuffled ones for sampling

[2] Note that we preserve the multihyperuniformity of the underlying point patterns by transforming them into equal-sized nonoverlapping disk packings [34].

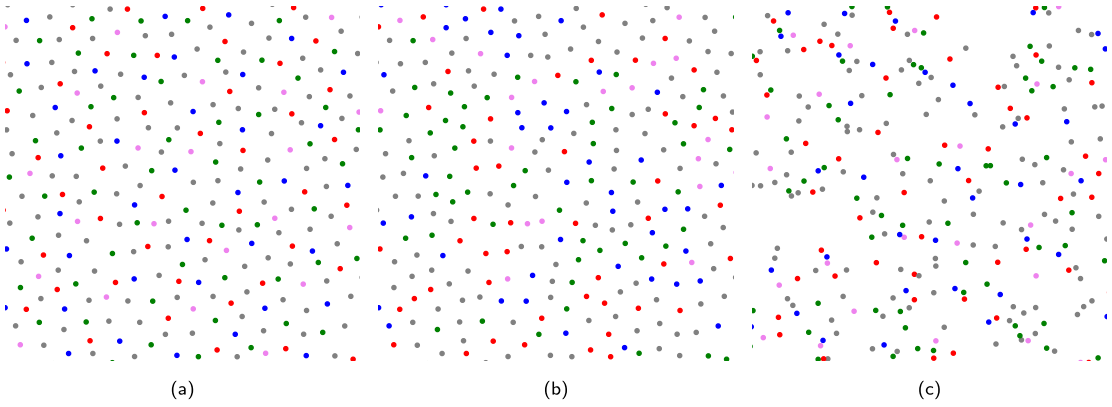



**Fig. 2.** Zoomed images of the avian retina system with (a) the original multihyperuniform order, as well as the same system with (b) the cell identities randomly shuffled, and (c) after equilibration using hard disk Monte Carlo moves. The red, blue, green, violet, and gray colored disks represent the red, blue, green, violet, and double photoreceptor cells, respectively. (For interpretation of the references to color in this figure legend, the reader is referred to the web version of this article.)

window radii greater than the mean inter-particle distance (i.e., $R \gtrsim 5a$) from the plots of the metric $\sigma_V^2(R)$ as a function of dimensionless sampling window radius $R/a$ in Fig. 3(a). The lower degree of mixing of the shuffled system is attributable to its clusters of like-species which are not observed in the unperturbed system. Note that a similar lack of clustering of like-species has also been observed in simulated multihyperuniform medium entropy alloys [61]. Windows smaller than this length scale will typically contain at most one cell, which is why the metric for the unperturbed and shuffled systems are identical for $R \lesssim 5a$. The inset plot in Fig. 3(a) highlights the class II hyperuniform and nonhyperuniform scalings in the large-$R$ asymptotic regimes of the unperturbed and shuffled systems, respectively. Thus, not only are the metrics for all cone types smaller in the multihyperuniform system when $R/a \gtrsim 5$, but they decay to zero in the large-$R$ asymptotic limit more quickly as well.

We observe similar differences between the mixing of the collective unperturbed and equilibrated systems in the plots of their metrics in Fig. 3(b). Specifically, $\sigma_V^2(R)$ for the hyperuniform unperturbed system is less than that of the nonhyperuniform equilibrated system for window sizes greater than a disk diameter (i.e., $R/a \gtrsim 2$). Note that this deviation of the metrics begins at a smaller length scale because of the relatively smaller average inter-particle distance in the equilibrated configurations.

To determine the entries of the mixing matrix $\mathcal{M}$, which is just a row vector for the time-independent avian systems, we set the small-, intermediate-, and large-length scales for the individual population systems as $R_s/a = 1$, $R_i/a = 10$, and $R_l/a = 25$, respectively. Those for the collective systems are respectively set as $R_s/a = 1$, $R_i/a = 5$, and $R_l/a = 15$. Note that the values of $R_s$ and $R_l$ are selected to represent the small-length roughly constant and large-length asymptotic decay regions of the metric, respectively. The values of $R_i$ are set slightly after the metrics for the unperturbed and perturbed systems start to deviate. The mixing matrices for the individual cell populations and collective patterns are listed row-wise in the top and bottom portions of Table 1, respectively. Overall, the trends shown in Table 1 are reflective of those seen in the plots of the full metric $\sigma_V^2(R)$.

**Table 1**
Entries of the mixing matrix $\mathcal{M}$ listed row-wise for (top) the five different cone types in the multihyperuniform (MHU) and shuffled avian retina configurations as well as the (bottom) collective hyperuniform (HU) and equilibrated (EQ) systems.

| Cone | $R_s = a$ | $R_i = 10a$ | $R_l = 25a$ |
|---|---|---|---|
| Violet (MHU) | $1.17 \times 10^{-3}$ | $1.80 \times 10^{-5}$ | $1.09 \times 10^{-6}$ |
| Violet (Shuffle) | $1.19 \times 10^{-3}$ | $2.31 \times 10^{-5}$ | $3.79 \times 10^{-6}$ |
| Blue (MHU) | $1.72 \times 10^{-3}$ | $2.10 \times 10^{-5}$ | $1.27 \times 10^{-6}$ |
| Blue (Shuffle) | $1.55 \times 10^{-3}$ | $3.01 \times 10^{-5}$ | $4.92 \times 10^{-6}$ |
| Green (MHU) | $2.06 \times 10^{-3}$ | $2.35 \times 10^{-5}$ | $1.53 \times 10^{-6}$ |
| Green (Shuffle) | $2.31 \times 10^{-3}$ | $4.16 \times 10^{-5}$ | $6.72 \times 10^{-6}$ |
| Red (MHU) | $1.85 \times 10^{-3}$ | $2.23 \times 10^{-5}$ | $1.39 \times 10^{-6}$ |
| Red (Shuffle) | $1.80 \times 10^{-3}$ | $3.42 \times 10^{-5}$ | $5.60 \times 10^{-6}$ |
| Double (MHU) | $4.41 \times 10^{-3}$ | $2.51 \times 10^{-5}$ | $2.24 \times 10^{-6}$ |
| Double (Shuffle) | $4.08 \times 10^{-3}$ | $6.36 \times 10^{-5}$ | $1.00 \times 10^{-5}$ |
| System | $R_s = a$ | $R_i = 5a$ | $R_l = 15a$ |
| Collective (HU) | $1.08 \times 10^{-2}$ | $4.35 \times 10^{-4}$ | $1.96 \times 10^{-5}$ |
| Collective (EQ) | $1.06 \times 10^{-2}$ | $7.77 \times 10^{-4}$ | $8.99 \times 10^{-5}$ |

### 5.2. Spinodal decomposition

In this subsection, we present numerical results for the mixing metric $\sigma_F^2(R,t)$ as calculated for the simulated spinodal decomposition patterns that were described in Section 3.2. In order to probe mixing up to large-length and long-time scales, we generate 10, $10^4 \times 10^4$ pixel systems that we simulate up to $10^6$ discrete time-steps. We use the pixel side-length $\ell$ as the characteristic length scale. To generate the initial configurations, the value of each pixel is sampled uniformly from the open interval $(-10^{-4}, 10^4)$. Sample images of simulated spinodal decomposition patterns at different times are shown in Fig. 4. We specifically compute the metric $\sigma_F^2(R,t)$ via the Fourier-space integral (11) using spectral densities $\tilde{\psi}(\mathbf{k})$ that were obtained with the fast Fourier transform algorithm. In the simulations of Eq. (23), we use diffusion coefficient $D = 0.01$ and length-scale $\gamma = 0.5$.

Generally, the system becomes more phase-separated across length scales over time, as seen in the plots of the metric as a function of dimensionless sampling window radius $R/\ell$ for various dimensionless times $Dt/\ell^2$ in Fig. 5(a). However, we note that the metric actually *decreases* in magnitude for window sizes greater than a pixel (i.e., $R/\ell \gtrsim 1$) during the first 0.1% of the total simulation time (i.e., $0 \lesssim Dt/\ell^2 \lesssim 10$). The large-$R$ asymptotic decay rate of the metric is nonhyperuniform (i.e., $\sigma_F^2(R,t) \propto 1/R^2$) during this relatively short time interval, but it abruptly increases to class I hyperuniform (i.e., $\sigma_F^2(R,t) \propto 1/R^3$) once $Dt/\ell^2 > 10$. Example images of nonhyperuniform and hyperuniform structures taken during this interval are shown in Figs. 4(a) and 4(b), respectively. During the subsequent, three-times longer interval $10 \lesssim Dt/\ell^2 \lesssim 40$, it is seen that the metric decays non-monotonically for $R/\ell \gtrsim 1$. We note that $\sigma_F^2(R)$ for stealthy hyperuniform Gaussian random fields obtained by superposition of random plane waves [124] exhibit similar non-monotonic decay [35]. Lastly, after only 0.5% of the total simulation time (i.e., $Dt/\ell^2 \sim 50$), the system enters the hyperuniform "scaling regime" during which the metric decays monotonically for relatively small window sizes (i.e., $R/\ell \gtrsim 5$). These hyperuniform late-time "scaling regime" spinodal decomposition patterns are more phase-separated than the hyperuniform intermediate-time ones, as seen in Fig. 4(c).

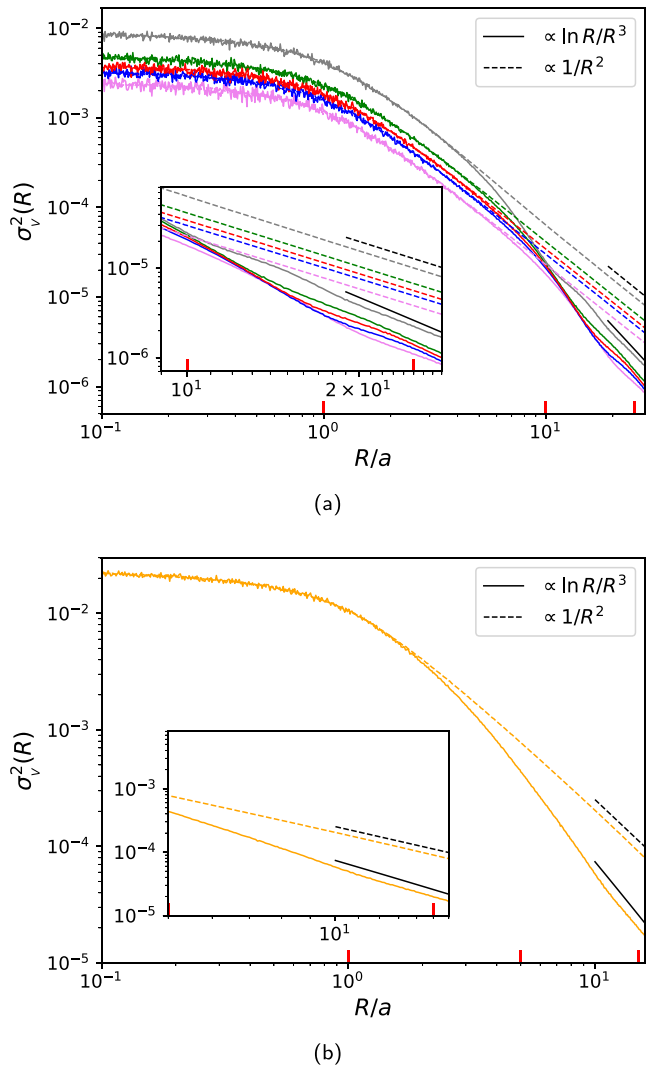



**Fig. 3.** Log–log plots of the mixing metric $\sigma_V^2(R)$ vs. dimensionless sampling window radius $R/a$ for (a) the 5 different cone species and (b) the collective system. Solid lines in (a) and (b) correspond to the unperturbed multihyperuniform system. Dashed lines in (a) correspond to the randomly shuffled configurations while those in (b) correspond to the equilibrated ones. In (a), the gray, green, red, blue and violet curves correspond to the double, green, red, blue, and violet cone types, respectively. The solid and dashed black lines highlight the class II hyperuniform and nonhyperuniform large-$R$ asymptotic scalings observed in the unperturbed and perturbed systems, respectively. The red tick marks in (a) and (b) denote our selected values of the length scales $R_{s/i/l}$ for these systems. (For interpretation of the references to color in this figure legend, the reader is referred to the web version of this article.)

We identify the most well-mixed structures to occur when $Dt/\ell^2 \sim 15$ via plots of the metric $\sigma_F^2(R,t)$ as a function of $Dt/\ell^2$ for various window sizes $R/\ell$ in Fig. 5(b). We note that such maximally-mixed structures occur at a time intermediate to $Dt/\ell^2 = 0$ and the onset of the "scaling regime" (i.e., $Dt/\ell^2 \sim 50$). This maximal-mixing is attributable to the combination of these systems' hyperuniformity and relative lack of phase-separation (see white-hued regions in Fig. 4(b).) It is also seen that the metric starts to increase across all length scales at the onset of the "scaling regime"; behavior that is consistent with phase-coarsening. Moreover, log–log regression of the metric for relatively large window sizes (e.g., $R/\ell \sim 200$), shows that $\sigma_F^2 \propto t^{1.08}$ ($R^2 = 0.99$). This observed power-law growth will be elaborated on further in Section 6.

To populate the entries of the mixing matrix $\mathcal{M}$, we set $R_s/\ell = 1$, $R_i/\ell = 10$, and $R_l/\ell = 100$ to represent the small-length roughly constant, intermediate-length fluctuating, and large-length asymptotic decay regions of the metric, respectively. Similarly, we set $Dt_s/\ell^2 = 0.5$, $Dt_i/\ell^2 = 15$, and $Dt_l/\ell^2 = 300$ to represent the short-time nonhyperuniform, intermediate-time most well-mixed, and long-time "scaling-regime' structures, respectively. Evaluating the metric at all 9 combinations of these length and time scales, we find that the spinodal mixing matrix is:

$$\mathcal{M}_S = \begin{bmatrix} 7.98\times10^{-2} & 1.26\times10^{-3} & 1.24\times10^{-5} \\ 5.75\times10^{-2} & 8.39\times10^{-5} & 9.42\times10^{-8} \\ 1.58 & 6.14\times10^{-2} & 5.56\times10^{-5} \end{bmatrix}. \tag{27}$$

As expected, the intermediate-time entries (middle row) are the smallest across all length scales. We also see that the bottom-left most entry $\sigma_F^2(R_s,t_l)$ is the largest in $\mathcal{M}_S$, reflecting the phase-separated structures that occur at long-times. However, since these "scaling regime" patterns are hyperuniform, they are slightly more well-mixed than the nonhyperuniform short-time structures across intermediate- and large-length scales. Lastly, the metric decreases from $R_s$ to $R_l$ for all time scales, reflecting the fact that even largely phase-separated systems will appear to be well-mixed when viewed from sufficiently large length scales.

We can use $\sigma_F^2(R,t)$ to identify sets of structures in the simulated $R/\ell$-$Dt/\ell^2$ plane that are (quantitatively) equally mixed as seen by the $\sigma_F^2 = 1.75$ "equimixing" contour plotted in the heatmap representation of the metric in Fig. 6(a). The small-window, short-time (i.e., $R/\ell = 35$, $Dt/\ell^2 = 30$) and the relatively large-window, long-time (i.e., $R/\ell = 260$, $Dt/\ell^2 = 250$) structures shown in Fig. 6(b) that were taken from the contour appear to be qualitatively equally phase-separated. In contrast, the small-window, long-time (i.e., $R/\ell = 35$, $Dt/\ell^2 = 250$) structure is relatively more phase-separated and thus has $\sigma_F^2 = 2.12$.

### 5.3. Baker's transformation

We devise here a new two-phase model system that undergoes an order–disorder transition upon repeated application of the baker's transformation. We use these structures to test the sensitivity of the metric $\sigma_V^2(R,t)$ to time-dependent changes mixing. To generate the time $t$ structure, we evolve an initial Poissonian (i.e., spatially uncorrelated) point pattern by the baker's map (25) $t$ times. These point patterns are represented as two-phase microstructures by taking their Voronoi tessellations under periodic boundary conditions and labeling (coloring) each cell according to the species of its generating point. Here, a Voronoi cell associated with any given point is the region of space closer to this point as measured by the Euclidean distance than to any other points, while the Voronoi tessellation is the collection of all such Voronoi cells [5].

Images shown in Fig. 7 show how this two-phase mixture evolves over time through a series of ordered and anisotropic striated structures (i.e., Figs. 7(a)–7(c)) to disordered and increasingly isotropic mixed ones (i.e., Figs. 7(d) and 7(e)). Unlike the perfectly rectangular striations present in previous implementations of the baker's map [98–100], the irregular boundaries of those in our model cause it to undergo the aforementioned order–disorder transition. Thus, this model system provides a platform for examining time-dependent structural transformations caused by mixing that we probe using the metric $\sigma_V^2(R,t)$.

We generated structures consisting of between $N = 1024$ and $N = 10^5$ total particles (Voronoi cells), with species 1 and 2 being present in nearly equal proportions. For each system size, 20 configurations were generated, each of which was simulated for 30 discrete time-steps (folds). Since the average cell area of these structures is $\langle A\rangle = 1/\rho$ [125], we use the characteristic length scale $a = \sqrt{\langle A\rangle} = 1/\sqrt{\rho}$ here. We compute $\sigma_V^2(R,t)$ for these simulated two-phase systems via the integral (7) using their spectral densities $\tilde{\chi}_V(\mathbf{k},t)$. Since each phase in these systems is represented by a set of non-overlapping convex

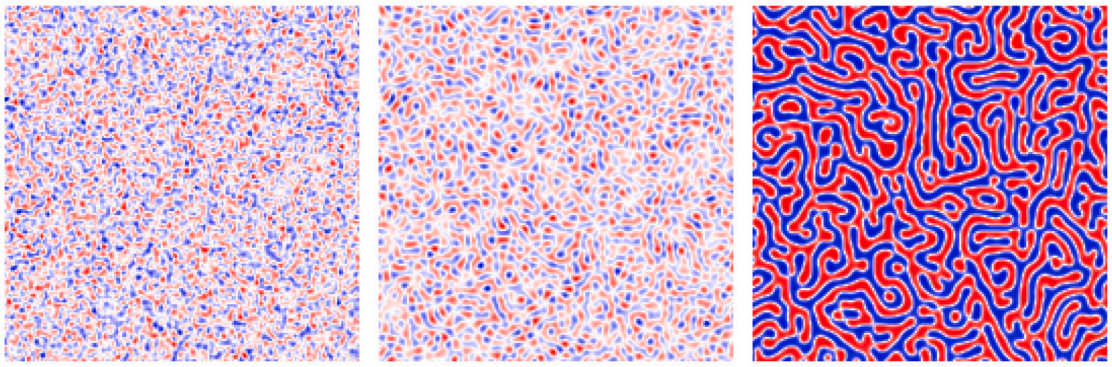



**Fig. 4.** Snapshots of the simulated spinodal decomposition pattern after (a) $Dt/\ell^2 = 0.5$, (b) $Dt/\ell^2 = 5$, and (c) $Dt/\ell^2 = 50$ dimensionless time steps in a square observation window with dimensionless side length $R/\ell = 175$. The dark blue and red colors correspond to regions of high-concentration of the two different solute species (phase-separated), while white regions have equal concentrations of each species (well-mixed). (For interpretation of the references to color in this figure legend, the reader is referred to the web version of this article.)

polygons, we specifically compute $\tilde{\chi}_V(\mathbf{k}, t)$ using the formulas derived in Ref. [126] (see Ref. [127] for specific implementation details).

Generally, we observe that the system becomes more mixed across length scales with each application of the baker's transformation, as indicated in the plots of the metric $\sigma_V^2(R, t)$ as a function of dimensionless window size $R\sqrt{\rho}$ for various times $t$ in Fig. 8. Specifically, for window sizes greater than half of the average cell-size (i.e., $R\sqrt{\rho} \gtrsim 0.15$) the metric decreases non-monotonically over half of the simulated time interval shown (i.e., $0 \leq t < 6$) – behavior that is attributable to the alternating red and blue striations present in the systems at these times. Moreover, the large-$R$ asymptotic decay regions of the metrics for the structures in this interval show class I hyperuniform scaling. Although the $t = 6$ structure still has striations (see Fig. 7(c)), and thus its metric decays non-monotonically, this system is not hyperuniform. This loss of hyperuniformity can be attributed to the presence of random substitutional defects[3] within the $t = 6$ system, i.e., red (blue) cells within a blue (red) striation.

During the second half of the simulated time interval (i.e., $7 \leq t \leq 12$), the striations disappear (see Figs. 7(d) and 7(e)), and thus the metric decays monotonically across all length scales during this interval. For $t > 7$, the metric does not change appreciably with respect to time — indicating that the system is not mixed further during this period. Thus, we define the "characteristic mixing time" $\tau_M$ to be the time when the striations first disappear, or equivalently, the time above which the system becomes mixing invariant. For this system with $N = 2^{16}$ cells, $\tau_M = 7$. How $\tau_M$ varies with respect to system size will be the subject of Section 5.4.

The destruction of hyperuniformity in this system is further highlighted in the plots of the angular-averaged spectral density $\tilde{\chi}_V(k, t)$ as a function of dimensionless wavenumber $k/\sqrt{\rho}$ in Fig. 9. Computing the hyperuniformity index $H(t)$ [cf. Eq. (21)] from these data, we specifically find that $H(t) \sim 10^{-4}$ over the first half of the simulation interval (i.e., $0 \leq t < 6$), while $1 < H(t) < 10^{-2}$ for the second half (i.e., $t \geq 6$). We also note that the Bragg peaks present in $\tilde{\chi}_V(k, t)$ over 75% of the simulated time interval (i.e., $0 \leq t \leq 8$) reflect the increasingly thinner striations in the systems during this period. Lastly, the directional-dependence of the Bragg peak locations seen in the inset plot of the 2D spectral density $\tilde{\chi}_V(\mathbf{k}, t = 2)$ quantitatively captures the structural anisotropy of the striated structures.

To fill the entries of the mixing matrix $\mathcal{M}$, we set the length scales $R_s/\ell = 1$, $R_i/\ell = 10$, and $R_l/\ell = 100$ using the same criteria as for the spinodal system. We set $t_s = 0$ to represent the most phase-separated structure, while $t_l = 10$ is chosen to represent the long-time mixing invariant structures. We set $t_i = 6$ since it is the last striated structure. We find that the mixing matrix for the baker's system is:

$$\mathcal{M}_B = \begin{bmatrix} 2.50 \times 10^{-1} & 2.47 \times 10^{-1} & 2.05 \times 10^{-1} \\ 2.23 \times 10^{-1} & 9.45 \times 10^{-2} & 1.00 \times 10^{-4} \\ 2.08 \times 10^{-1} & 6.12 \times 10^{-2} & 2.55 \times 10^{-4} \end{bmatrix}. \tag{28}$$

Interestingly, we see from $\mathcal{M}_B$ that the final-striated structure (middle row) is slightly more well-mixed than the mixing invariant one (bottom row) for $R_l$. Thus, while the disorder of the long-time systems makes them more well-mixed at small- and intermediate-length scales, the relatively more-ordered last striated structure is more well-mixed at large-length scales.

### 5.4. Characteristic mixing times for the Baker's transformation

In this subsection, we use simple geometrical arguments to derive an equation for the characteristic mixing time as a function of system size $N$, i.e., $\tau_M(N)$. We support these analytical predictions by numerically estimating $\tau_M(N)$ from simulated systems using our metric.

To begin, the $N$-particle Poisson point patterns used to generate the two-phase baker's systems have fixed simulation box side lengths $L = \sqrt{N/\rho}$. While the striation thickness in the two-phase systems varies along the horizontal direction due to the irregularity of the Voronoi cells' shapes, sizes and positions, the average thickness as a function of time $l(t)$ may be approximated as

$$l(t) = \frac{L}{2^{t+1}} = \frac{\sqrt{N}}{2^{t+1}\sqrt{\rho}}. \tag{29}$$

Since the distribution of points within each striation remains Poissonian for all times, the average Voronoi cell size within a striation is time-independent, i.e., $a(t) = a = 1/\sqrt{\rho}$. Note that the boundary irregularities always cause red (blue) cells to penetrate the edges of the blue (red) striations. Thus, we hypothesize that the presence of such substitutional defects will cause the striations to disappear when their thickness is equal to the average cell size. Solving $l(\tau_M) = a$ for the characteristic mixing time $\tau_M$ results in the equation

$$\tau_M(N) = \frac{\ln N}{2 \ln 2} - 1. \tag{30}$$

From Eq. (30), we see that $\tau_M$ grows logarithmically in $N$. In order to make predictions about $\tau_M$ for simulated systems, which are only defined at integer values of time $t$, we consider Eq. (30) rounded up and down to the nearest integer via the ceiling $\lceil x \rceil$ and floor $\lfloor x \rfloor$ functions, respectively. We test the accuracy of Eq. (30) by

[3] Note that in Ref. [128], it was shown via theory and simulation that the hyperuniformity of crystalline point patterns is degraded/destroyed by substitutional defects.

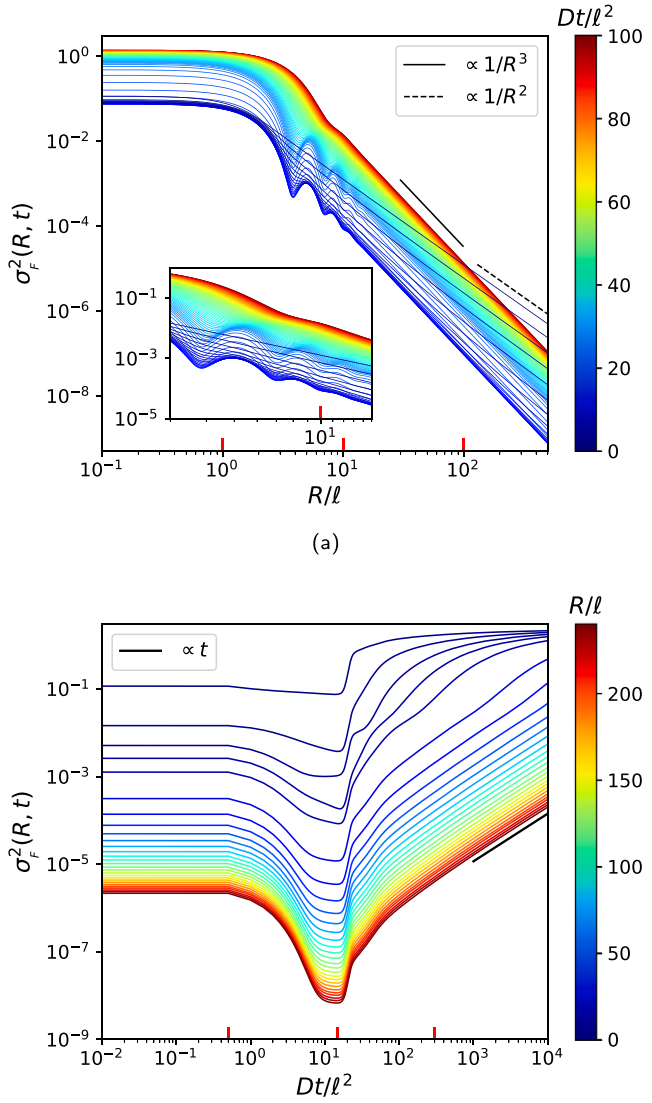



**Fig. 5.** Log–log plots of the mixing metric $\sigma_F^2(R,t)$ as a function of (a) dimensionless distance $R/\ell$ for various dimensionless times $Dt/\ell^2$ and (b) $Dt/\ell^2$ for various values of $R/\ell$. In (a), the solid and dashed black lines highlight the observed hyperuniform and nonhyperuniform large-$R$ asymptotic scaling behaviors of the metric, respectively. While we simulated up to dimensionless time $Dt/\ell^2 = 10^4$, only the first 1% of this interval is shown in (a) since the most appreciable changes in the metric occur here. In (b), the solid black line highlights the observed power-law growth of the metric in the long-time asymptotic limit. The red tick marks in (a) and (b) denote our selected values of length $R_{s/i/l}$ and time $t_{s/i/l}$ scales, respectively. (For interpretation of the references to color in this figure legend, the reader is referred to the web version of this article.)

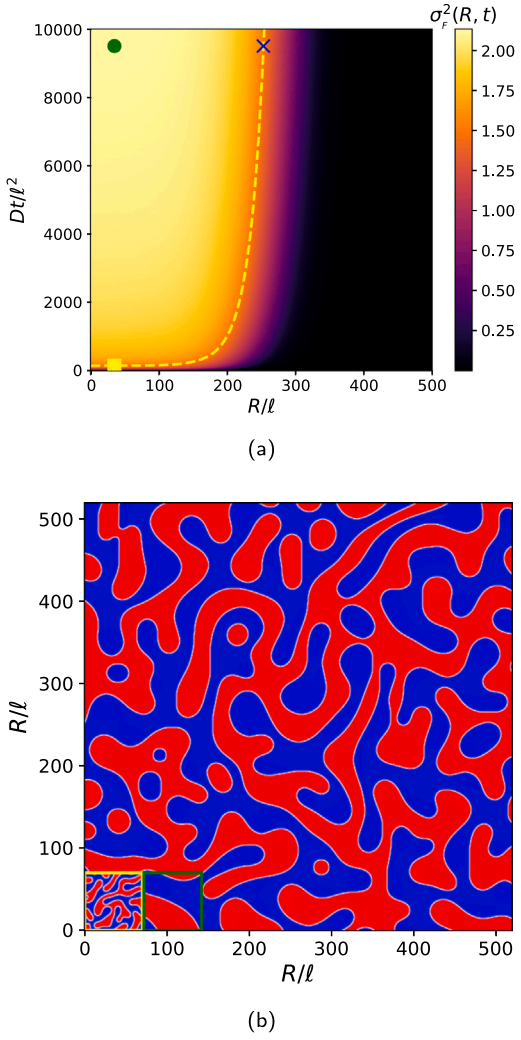



**Fig. 6.** Images of (a) a heatmap representing values of $\sigma_F^2(R,t)$ as a function of dimensionless time $Dt/\ell^2$ and distance $R/\ell$, and (b) sample images of the spinodal decomposition pattern at lengths and times corresponding the scatter plot points in (a). The dashed yellow line in (a) encompasses all simulated structures with $\sigma_F^2 = 1.75$. The large, outer configuration in (b) corresponds to the blue 'X' in (a); the small, superimposed configuration in the yellow box in (b) corresponds to the yellow box in (a); the small portion of the large configuration in the green box in (b) corresponds to the green circle in (a). Note that in (b), although $R$ corresponds to the circular sampling window radius, we have chosen to show square snapshots with side lengths equal to $2R$ to facilitate viewing. (For interpretation of the references to color in this figure legend, the reader is referred to the web version of this article.)

determining it numerically from simulated systems using our mixing metric. We specifically estimate $\tau_M$ to be the time at which $\sigma_V^2(R,t)$ becomes monotonically decreasing, as this behavior correlates with the disappearance of striations and can be determined numerically by the condition

$$\left.\frac{\partial \sigma_V^2(R,t)}{\partial R}\right|_{t=\tau_M} < \epsilon \quad \forall R. \tag{31}$$

Here, we set the numerical tolerance $\epsilon = 10^{-5}$.

It is seen that $\lfloor \tau_M(N) \rfloor$, as predicted theoretically by relation (30), correlates almost exactly with the numerical estimates of $\tau_M$ shown in the plots of $\tau_M(N)$, $\lceil \tau_M(N) \rceil$ and $\lfloor \tau_M(N) \rfloor$ in Fig. 10. The one exception to this trend occurs when $N = 6 \times 10^4$, for which $\tau_M(N) \approx 6.94$ and we observe that $\tau_M = 7$. By definition, $l(\lfloor \tau_M(N) \rfloor)$ and $l(\lceil \tau_M(N) \rceil)$ should be slightly larger and smaller than the average cell size $a$, respectively. Thus, the fact that $\lfloor \tau_M(N) \rfloor$ provides the most accurate predictions for $\tau_M$ suggests that $l(t)$ as given by Eq. (29) is a slight overestimation of the true striation thickness. Exact agreement between Eq. (30) and the measured $\tau_M$ is seen for system sizes $N = 2^{10}, 2^{12}, 2^{14}$, and $2^{16}$. This result is consistent with the fact that Eq. (30) takes on integer values for $N = 2^{2n}$, where $n \in \mathbb{Z}$.

Lastly, we note that for general systems in dimension $d \geq 2$ consisting of $P \geq 2$ distinct layered phases, the formula for $\tau_M(N)$ becomes

$$\tau_M(N; P, d) = \frac{\ln N}{d \ln P} - 1. \tag{32}$$

For these systems, $\tau_M(N; P, d)$ will have integer values for system sizes of the form $N = P^{dn}$. Furthermore, taking the thermodynamic limit of Eq. (32), in which $N, L \to \infty$ while $\rho$ is constant, results in a divergent

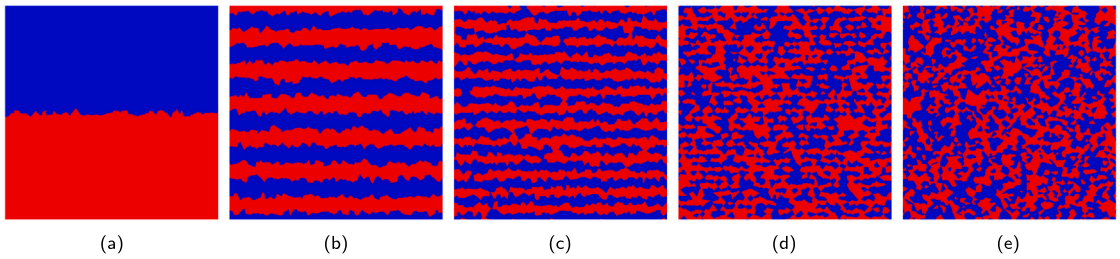



**Fig. 7.** Images of an (a) initially phase-separated two-phase material microstructure ($t = 0$), the same microstructure after (b) 5 ($t = 5$), (c) 6 ($t = 6$), (d) 7 ($t = 7$), and (e) ($t = 8$) applications of the baker's transformation. The zoomed-in snapshots shown in (a)–(e) are taken from systems consisting of $N = 2^{16}$ Voronoi cells.

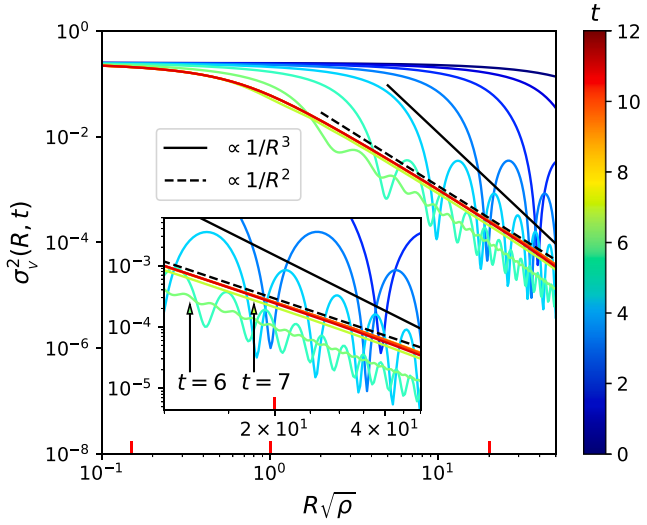



**Fig. 8.** Log–log plots of the mixing metric $\sigma_v^2(R,t)$ as a function of dimensionless sampling window radius $R\sqrt{\rho}$ for the baker's transformation system at times $t = 0, 1, \ldots, 12$. This range of times was selected because the metric does not change appreciably across length scales for times $t > 8$. The inset plot highlights the large-$R$ asymptotic hyperuniform (solid black) and nonhyperuniform (dashed black) scalings of the mixing metric observed here. The red tick marks on the horizontal axis denote our selected values of the length scales $R_{s/i/l}$.

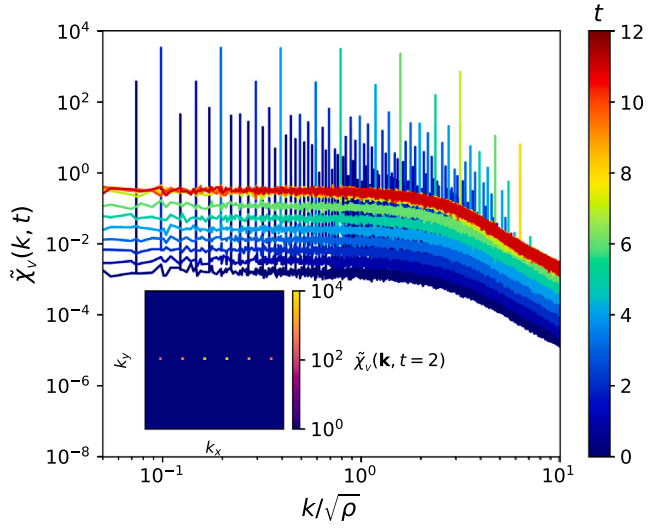



**Fig. 9.** Log–log plots of the angular-averaged spectral density $\tilde{\chi}_v(k)$ vs dimensionless wavenumber $k/\sqrt{\rho}$ for the baker's transformation system at times $t = 0, 1, \ldots, 12$. The inset plot is of the full two-dimensional spectral density of the system at $t = 2$.

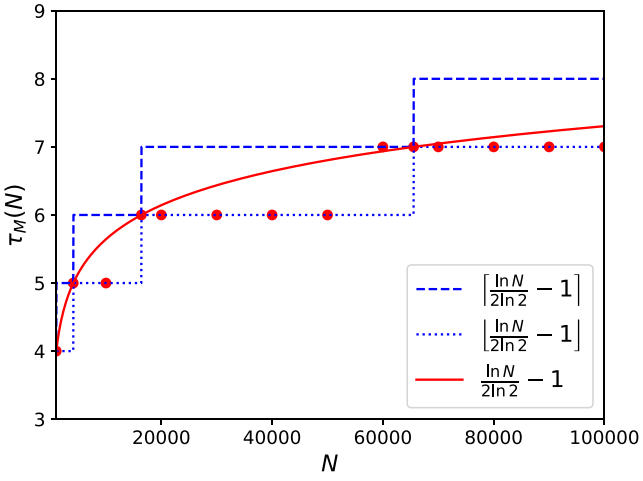



**Fig. 10.** Plots of the characteristic mixing time $\tau_M$ as a function of the number of cells (particles) in the system $N$. The solid red line is the theoretical prediction of $\tau_M(N)$ given by Eq. (30), while the dashed and dotted blue lines correspond to $\lceil \tau_M(N) \rceil$ and $\lfloor \tau_M(N) \rfloor$, respectively. The red scatter plot points are values of $\tau_M$ that were obtained numerically from the simulated systems using the inequality (31). Note the excellent prediction of Eq. (30) as compared to numerics. (For interpretation of the references to color in this figure legend, the reader is referred to the web version of this article.)

characteristic mixing time. Thus, in this limit, the striations will never disappear because their thickness $l(t) \to \infty \quad \forall t$ while the cell-size $a$ remains finite.

## 6. Conclusions

In summary, we have demonstrated that the mixing metric $\sigma_{V/F}^2(R,t)$ and matrix $\mathcal{M}$ are sensitive quantitative measures of mixing for three representative complex model microstructures across both length and time scales. Through application of $\sigma_V^2(R)$ and $\mathcal{M}$ to the avian system, we observed that the simultaneous hyperuniformity of the individual phases in multihyperuniform microstructures makes them overall more well-mixed across nearly all length scales than those in nonhyperuniform multi-phase systems. Moreover, such superior mixing is coincident with an observed lack of clustering of like-phases in multihyperuniform systems. Additionally, the metrics $\sigma_F^2(R,t)$ and $\mathcal{M}$ identified previously uncharacterized intermediate-time hyperuniform spinodal decomposition patterns that are more well-mixed across virtually all length scales than the short-time nonhyperuniform and late-time hyperuniform "scaling regime" ones. The high-degree of mixing in these structures is attributable to their hyperuniformity and overall lack of phase separation. We also observed that the metric grows linearly in time for large window sizes $R \gtrsim R_l$ during the "scaling regime". Lastly, application of $\sigma_V^2(R,t)$ and $\mathcal{M}$ to the new two-phase model system revealed that the presence of any disorder in a finite-sized system undergoing the baker's transformation can cause it to not be mixed further after a finite "characteristic mixing time". Since experimental

systems are finite-sized and will inevitably possess some disorder, this behavior could be an important consideration when using the baker's transformation to manufacture materials.

We note that the superior mixing of multihyperuniform systems makes them potentially desirable for applications in which spatially uniform distributions of all phases across all length scales correlates with desirable physical properties. One such example being certain computationally designed stealthy multihyperuniform medium-entropy alloys, which were shown to have larger electronic band gaps and superior thermal transport properties than those observed in nonhyperuniform model alloys [61]. Interestingly, the non-monotonic decay of the metric for intermediate-time hyperuniform spinodal structures is typically observed in ordered and disordered stealthy hyperuniform two-phase microstructures [28] and scalar fields [35]. Thus, future work might consider leveraging spinodal decomposition phenomena to create stealthy hyperuniform materials, which are known to exhibit exotic physical properties [67–70,83,129]. Future research could also examine the origins of the power-law growth of the metric for large window sizes during the "scaling regime". In addition to examining multi-phase generalizations of the two-phase model baker's transformation system in 2D and 3D, it would be interesting to study how the mixing behaviors of this system change as the underlying point pattern becomes increasingly correlated. Such explorations could determine if hyperuniform point patterns produce hyperuniform mixing invariant structures, and thus possibly guide the fabrication of hyperuniform materials.

Beyond the multi-phase and scalar field microstructures examined here, one could generalize our metric to characterize mixing in vector fields. Such a metric would quantify fluctuations in local orientational homogeneity and could be applied to, for example, the director fields of liquid crystalline materials [95], or the "spin microemulsions" that were recently observed in certain simulated Bose–Einstein condensates [130]. Since $\sigma^2_{V/F}(R,t)$ can be computed directly from scattering data, it could be used to quantify mixing in 3D systems whose internal microstructures cannot be resolved using microscopy techniques, such as medium- and high-entropy alloys [11]. We note that in Ref. [131], $\sigma^2_V(R)$ was computed from small angle X-ray scattering data for certain porous silicas, aerogels, and semicrystalline polyethylene.

Another potentially fruitful area of future research is applying our mixing metric to the inverse problem of designing a material whose bulk physical properties are tuned via specific length-dependent mixing properties. Specifically, one could devise a realizable $\sigma^2_{V/F}(R)$ with prescribed small-, intermediate-, and large-length scale mixing qualities, and then generate the corresponding microstructure using inverse methods described in Refs. [86,132]. One could also use our mixing metric to design materials with novel bulk properties by tuning the mixing characteristics of the microstructures in both space and time. While the computational cost of devising and constraining a realizable $\sigma^2_F(R,t)$ for this problem would be prohibitively high, one could reduce this cost by only targeting the 9 entries of the mixing matrix $\mathcal{M}$. From here, a numerical optimization algorithm could be used to determine the specific free energy density $f(c)$ that satisfies the prescribed mixing matrix. Finally, the metric $\sigma^2_F(R,t)$ could be used to the characterize mixing behaviors in this designed microstructure across both length and time scales.

## Declaration of competing interest

The authors declare that they have no known competing financial interests or personal relationships that could have appeared to influence the work reported in this paper.

## Acknowledgments

This work was sponsored by the Army Research Office, United States and was accomplished under Cooperative Agreement Number W911NF-22-2-0103, as well as the Air Force Office of Scientific Research Program under award No. FA9550-18-1-0514. The authors thank the Princeton Institute for Computational Science and Engineering (PICSciE) for the computational resources.

## References

[1] P.V. Danckwerts, The definition and measurement of some characteristics of mixtures, Appl. Sci. Res., Sect. A 3 (4) (1952) 279–296.
[2] R.M. Christensen, Mechanics of Composite Materials, Wiley, New York, 1979.
[3] J. Chen, M.F. Thorpe, L.C. Davis, Elastic properties of rigid fiber-reinforced composites, J. Appl. Phys. 77 (1995) 4349–4360.
[4] J.M. Ottino, D.V. Khakhar, Mixing and segregation of granular materials, Annu. Rev. Fluid Mech. 32 (1) (2000) 55–91.
[5] S. Torquato, Random Heterogeneous Materials: Microstructure and Macroscopic Properties, Springer-Verlag, New York, 2002.
[6] G.W. Milton, The Theory of Composites, Cambridge University Press, Cambridge, England, 2002.
[7] M. Sahimi, Heterogeneous Materials I: Linear Transport and Optical Properties, Springer-Verlag, New York, 2003.
[8] V.A. Buryachenko, Micromechanics of Heterogeneous Materials, Springer, US, 2007.
[9] G. Ristow, Pattern Formation in Granular Materials, in: Springer Tracts in Modern Physics, vol. 164, Springer, Berlin, Heidelberg, 2000.
[10] S. Torquato, Perspective: Basic understanding of condensed phases of matter via packing models, J. Chem. Phys. 149 (2018) 020901.
[11] E.P. George, D. Raabe, R.O. Ritchie, High-entropy alloys, Nat. Rev. Mater. 4 (8) (2019) 515–534.
[12] B.A. Connor, R.W. Smaha, J. Li, A. Gold-Parker, A.J. Heyer, M.F. Toney, Y.S. Lee, H.I. Karunadasa, Alloying a single and a double perovskite: a $Cu^{+/2+}$ mixed-valence layered halide perovskite with strong optical absorption, Chem. Sci. 12 (2021) 8689–8697.
[13] S. Wilken, A. Chaderjian, O.A. Saleh, Spatial organization of phase-separated DNA droplets, Phys. Rev. X 13 (3) (2023) 031014, publisher: American Physical Society.
[14] P.J. Flory, Thermodynamics of high polymer solutions, J. Chem. Phys. 10 (1) (1942) 51–61.
[15] M.L. Huggins, Solutions of long chain compounds, J. Chem. Phys. 9 (5) (1941) 440.
[16] W. Wu, M. Singh, A. Masud, X. Wang, A. Nallapaneni, Z. Xiao, Y. Zhai, Z. Wang, T. Terlier, M. Bleuel, G. Yuan, S.K. Satija, J.F. Douglas, K. Matyjaszewski, M.R. Bockstaller, A. Karim, Control of phase morphology of binary polymer grafted nanoparticle blend films via direct immersion annealing, ACS Nano 15 (7) (2021) 12042–12056.
[17] Z. Peng, N. Stingelin, H. Ade, J.J. Michels, A materials physics perspective on structure–processing–function relations in blends of organic semiconductors, Nat. Rev. Mater. 8 (7) (2023) 439–455.
[18] A.K. Sen, S. Torquato, Effective conductivity of anisotropic two-phase composite media, Phys. Rev. B 39 (1989) 4504–4515.
[19] B.-J. Hwang, L.S. Sarma, J.-M. Chen, C.-H. Chen, S.-C. Shih, G.-R. Wang, D.-G. Liu, J.-F. Lee, M.-T. Tang, Structural models and atomic distribution of bimetallic nanoparticles as investigated by X-ray absorption spectroscopy, J. Am. Chem. Soc. 127 (31) (2005) 11140–11145.
[20] A.-P. Hynninen, J.H.J. Thijssen, E.C.M. Vermolen, M. Dijkstra, A. Van Blaaderen, Self-assembly route for photonic crystals with a bandgap in the visible region, Nature Mater. 6 (2007) 202.
[21] G. Santagiuliana, O.T. Picot, M. Crespo, H. Porwal, H. Zhang, Y. Li, L. Rubini, S. Colonna, A. Fina, E. Barbieri, A.B. Spoelstra, G. Mirabello, J.P. Patterson, L. Botto, N.M. Pugno, T. Peijs, E. Bilotti, Breaking the nanoparticle loading–dispersion dichotomy in polymer nanocomposites with the art of croissant-making, ACS Nano 12 (9) (2018) 9040–9050.
[22] N. Meng, X. Ren, G. Santagiuliana, L. Ventura, H. Zhang, J. Wu, H. Yan, M.J. Reece, E. Bilotti, Ultrahigh $\beta$-phase content poly(vinylidene fluoride) with relaxor-like ferroelectricity for high energy density capacitors, Nature Commun. 10 (1) (2019) 4535.
[23] S. Torquato, J. Kim, Nonlocal effective electromagnetic wave characteristics of composite media: Beyond the quasistatic regime, Phys. Rev. X 11 (2021) 021002.
[24] C.M. Heil, A. Patil, B. Vanthournout, S. Singla, M. Bleuel, J.-J. Song, Z. Hu, N.C. Gianneschi, M.D. Shawkey, S.K. Sinha, A. Jayaraman, A. Dhinojwala, Mechanism of structural colors in binary mixtures of nanoparticle-based supraballs, Sci. Adv. 9 (21) (2023) eadf2859.

[25] J. Li, R. Matheu, F. Ke, Z. Liu, Y. Lin, H.I. Karunadasa, Mosaic $Cu^{I}$–$Cu^{II}$–$In^{III}$ 2d perovskites: Pressure-dependence of the intervalence charge transfer and a mechanochemical alloying method, Angew. Chem. Int. Ed. 62 (20) (2023) e202300957.

[26] Y.A. Kram, S. Mantey, J.C. Corbo, Avian cone photoreceptors tile the retina as five independent, self-organizing mosaics, PLoS One 5 (2010) e8992.

[27] Q. Ma, Y. Song, W. Sun, J. Cao, H. Yuan, X. Wang, Y. Sun, H.C. Shum, Cell-inspired all-aqueous microfluidics: From intracellular liquid–liquid phase separation toward advanced biomaterials, Adv. Sci. 7 (7) (2020) 1903359.

[28] S. Torquato, M. Skolnick, J. Kim, Local order metrics for two-phase media across length scales, J. Phys. A 55 (27) (2022) 274003.

[29] E. Komatsu, A. Kogut, M.R. Nolta, C.L. Bennett, M.H. i, G. Hinshaw, N. Jarosik, M. Limon, S.S. Meyer, L. Page, D.N. Spergel, G.S. Tucker, L. Verde, E. Wollack, E.L. Wright, First-year Wilkinson microwave anisotropy probe (WMAP) observations: Tests of Gaussianity, Astrophys. J. Suppl. Ser. 148 (2003) 119.

[30] B.L. Lu, S. Torquato, Local volume fraction fluctuations in heterogeneous media, J. Chem. Phys. 93 (1990) 3452–3459.

[31] J. Quintanilla, S. Torquato, Local volume fraction fluctuations in random media, J. Chem. Phys. 106 (1997) 2741–2751.

[32] J. Quintanilla, S. Torquato, Local volume fraction fluctuations in periodic heterogeneous media, J. Chem. Phys. 110 (1999) 3215–3219.

[33] C.E. Zachary, S. Torquato, Hyperuniformity in point patterns and two-phase heterogeneous media, J. Stat. Mech.: Theory Exp. 2009 (2009) P12015.

[34] S. Torquato, Hyperuniformity and its generalizations, Phys. Rev. E 94 (2016) 022122.

[35] Z. Ma, S. Torquato, Random scalar fields and hyperuniformity, J. Appl. Phys. 121 (2017) 244904.

[36] L.T. Fan, Y. m. Chen, F.S. Lai, Recent developments in solids mixing, Powder Technol. 61 (3) (1990) 255–287.

[37] C.F. Schreck, C.S. O'Hern, L.E. Silbert, Tuning jammed frictionless disk packings from isostatic to hyperstatic, Phys. Rev. E 84 (2011) 011305.

[38] D.O. Dumcenco, H. Kobayashi, Z. Liu, Y.-S. Huang, K. Suenaga, Visualization and quantification of transition metal atomic mixing in $Mo_{1-x}W_xS_2$ single layers, Nature Commun. 4 (1) (2013) 1351.

[39] P.M.C. Lacey, Developments in the theory of particle mixing, J. Appl. Chem. 4 (5) (1954) 257–268.

[40] S. Torquato, Hyperuniform states of matter, Phys. Rep. 745 (2018) 1–95.

[41] M. Camesasca, M. Kaufman, I. Manas-Zloczower, Quantifying fluid mixing with the Shannon entropy, Macromol. Theory Simul. 15 (8) (2006) 595–607.

[42] M. Camesasca, I. Manas-Zloczower, Danckwerts revisited – the use of entropy to define scale and intensity of segregation, Macromol. Theory Simul. 18 (2) (2009) 87–96.

[43] NASA/WMAP Science Team, Nine year microwave sky, 2014.

[44] S. Torquato, F.H. Stillinger, Local density fluctuations, hyperuniform systems, and order metrics, Phys. Rev. E 68 (2003) 041113.

[45] M. Florescu, S. Torquato, P.J. Steinhardt, Complete band gaps in two-dimensional photonic quasicrystals, Phys. Rev. B 80 (2009) 155112.

[46] Y. Jiao, T. Lau, H. Hatzikirou, M. Meyer-Hermann, J.C. Corbo, S. Torquato, Avian photoreceptor patterns represent a disordered hyperuniform solution to a multiscale packing problem, Phys. Rev. E 89 (2014) 022721.

[47] C. De Rosa, F. Auriemma, C. Diletto, R. Di Girolamo, A. Malafronte, P. Morvillo, G. Zito, G. Rusciano, G. Pesce, A. Sasso, Toward hyperuniform disordered plasmonic nanostructures for reproducible surface-enhanced Raman spectroscopy, Phys. Chem. Chem. Phys. 17 (2015) 8061–8069.

[48] O. Leseur, R. Pierrat, R. Carminati, High-density hyperuniform materials can be transparent, Optica 3 (2016) 763–767.

[49] T. Ma, H. Guerboukha, M. Girard, A.D. Squires, R.A. Lewis, M. Skorobogatiy, 3D printed hollow-core terahertz optical waveguides with hyperuniform disordered dielectric reflectors, Adv. Opt. Mater. 4 (2016) 2085–2094.

[50] L.S. Froufe-Pérez, M. Engel, J. José Sáenz, F. Scheffold, Transport phase diagram and Anderson localization in hyperuniform disordered photonic materials, Proc. Natl. Acad. Sci. 114 (2017) 9570–9574.

[51] A. Chremos, J.F. Douglas, Particle localization and hyperuniformity of polymer-grafted nanoparticle materials, Ann. Phys. 529 (2017).

[52] A. Chremos, J.F. Douglas, Hidden hyperuniformity in soft polymeric materials, Phys. Rev. Lett. 121 (2018) 258002.

[53] H. Zhang, H. Chu, H. Giddens, W. Wu, Y. Hao, Experimental demonstration of luneburg lens based on hyperuniform disordered media, Appl. Phys. Lett. 114 (2019) 053507.

[54] F. Sgrignuoli, L. Dal Negro, Hyperuniformity and wave localization in pinwheel scattering arrays, Phys. Rev. B 103 (2021) 224202.

[55] F. Sgrignuoli, S. Torquato, L. Dal Negro, Subdiffusive wave transport and weak localization transition in three-dimensional stealthy hyperuniform disordered systems, Phys. Rev. B 105 (2022) 064204.

[56] A. Rohfritsch, J.-M. Conoir, T. Valier-Brasier, R. Marchiano, Impact of particle size and multiple scattering on the propagation of waves in stealthy-hyperuniform media, Phys. Rev. E 102 (2020) 053001.

[57] H. Zhang, Q. Cheng, H. Chu, O. Christogeorgos, W. Wu, Y. Hao, Hyperuniform disordered distribution metasurface for scattering reduction, Appl. Phys. Lett. 118 (2021) 101601.

[58] Y. Zheng, D. Chen, L. Liu, Y. Liu, M. Chen, H. Zhuang, Y. Jiao, Topological transformations in hyperuniform pentagonal two-dimensional materials induced by stone-wales defects, Phys. Rev. B 103 (2021) 245413.

[59] D. Chen, Y. Zheng, C.-H. Lee, S. Kang, W. Zhu, H. Zhuang, P. Huang, Y. Jiao, Nearly hyperuniform, nonhyperuniform, and antihyperuniform density fluctuations in two-dimensional transition metal dichalcogenides with defects, Phys. Rev. B 103 (2021) 224102.

[60] D. Chen, Y. Zheng, L. Liu, G. Zhang, M. Chen, Y. Jiao, H. Zhuang, Stone–wales defects preserve hyperuniformity in amorphous two-dimensional networks, Proc. Natl. Acad. Sci. 118 (2021) e2016862118.

[61] D. Chen, X. Jiang, D. Wang, J. Vidallon, H. Zhuang, Y. Jiao, Multihyperuniform long-range order in medium-entropy alloys, Acta Mater. 246 (2023) 118678.

[62] N. Granchi, R. Spalding, M. Lodde, M. Petruzzella, F. Otten, A. Fiore, F. Intonti, R. Sapienza, M. Florescu, M. Gurioli, Near-field investigation of luminescent hyperuniform disordered materials, Adv. Opt. Mater. 10 (8) (2022) 2102565.

[63] S. Aeby, G. Aubry, L. Froufe-Pérez, F. Scheffold, Fabrication of hyperuniform dielectric networks via heat-induced shrinkage reveals a bandgap at telecom wavelengths, Adv. Opt. Mater. 10 (14) (2022) 2200232.

[64] P.M. Piechulla, R.B. Wehrspohn, A.N. Sprafke, Toward hyperuniform disorder via self-assembly of bidisperse colloidal patterns at an electrode, Adv. Mater. Interfaces 10 (3) (2023) 2201395.

[65] J.R. Dale, J.D. Sartor, R.C. Dennis, E.I. Corwin, Hyperuniform jammed sphere packings have anomalous material properties, Phys. Rev. E 106 (2022) 024903.

[66] J. Puig, F. Elías, J. Aragón Sánchez, R. Cortés Maldonado, G. Rumi, G. Nieva, P. Pedrazzini, A.B. Kolton, Y. Fasano, Anisotropic suppression of hyperuniformity of elastic systems in media with planar disorder, Commun. Mater. 3 (1) (2022) 32.

[67] M. Florescu, S. Torquato, P.J. Steinhardt, Designer disordered materials with large complete photonic band gaps, Proc. Natl. Acad. Sci. 106 (2009) 20658–20663.

[68] W. Man, M. Florescu, K. Matsuyama, P. Yadak, G. Nahal, S. Hashemizad, E. Williamson, P. Steinhardt, S. Torquato, P. Chaikin, Photonic band gap in isotropic hyperuniform disordered solids with low dielectric contrast, Opt. Express 21 (2013) 19972–19981.

[69] G. Gkantzounis, T. Amoah, M. Florescu, Hyperuniform disordered phononic structures, Phys. Rev. B 95 (2017) 094120.

[70] S. Yu, C.-W. Qiu, Y. Chong, S. Torquato, N. Park, Engineered disorder in photonics, Nat. Rev. Mater. 6 (2021) 226–243.

[71] M. Klatt, P. Steinhardt, S. Torquato, Wave propagation and band tails of two-dimensional disordered systems in the thermodynamic limit, Proc. Natl. Acad. Sci. 119 (52) (2022) e2213633119.

[72] S. Torquato, D. Chen, Multifunctional hyperuniform cellular networks: optimality, anisotropy and disorder, Multifunct. Mater. 1 (2018) 015001.

[73] J. Kim, S. Torquato, Multifunctional composites for elastic and electromagnetic wave propagation, Proc. Natl. Acad. Sci. 117 (2020) 8764–8774.

[74] J. Kim, S. Torquato, Effective elastic wave characteristics of composite media, New J. Phys. 22 (2020) 123050.

[75] S. Torquato, Extraordinary disordered hyperuniform multifunctional composites, J. Compos. Mater. 56 (23) (2022) 3635–3649.

[76] R. Degl'Innocenti, Y.D. Shah, L. Masini, A. Ronzani, A. Pitanti, Y. Ren, D.S. Jessop, A. Tredicucci, H.E. Beere, D.A. Ritchie, Hyperuniform disordered terahertz quantum cascade laser, Sci. Rep. 6 (2016) 19325.

[77] W. Zhou, Z. Cheng, B. Zhu, X. Sun, H.K. Tsang, Hyperuniform disordered network polarizers, IEEE J. Sel. Top. Quantum Elec. 22 (2016) 288–294.

[78] F. Bigourdan, R. Pierrat, R. Carminati, Enhanced absorption of waves in stealth hyperuniform disordered media, Opt. Express 27 (2019) 8666–8682.

[79] S. Gorsky, W.A. Britton, Y. Chen, J. Montaner, A. Lenef, M. Raukas, L. Dal Negro, Engineered hyperuniformity for directional light extraction, APL Photonics 4 (2019) 110801.

[80] A. Sheremet, R. Pierrat, R. Carminati, Absorption of scalar waves in correlated disordered media and its maximization using stealth hyperuniformity, Phys. Rev. A 101 (2020) 053829.

[81] R. Lin, V. Mazzone, N. Alfaraj, J. Liu, X. Li, A. Fratalocchi, On-chip hyperuniform lasers for controllable transitions in disordered systems, Laser Photonics Rev. 14 (2) (2020) 1800296.

[82] L.S. Froufe-Pérez, G.J. Aubry, F. Scheffold, S. Magkiriadou, Bandgap fluctuations and robustness in two-dimensional hyperuniform dielectric materials, Opt. Express 31 (11) (2023) 18509–18515.

[83] J. Kim, S. Torquato, Effective electromagnetic wave properties of disordered stealthy hyperuniform layered media beyond the quasistatic regime, Optica 10 (8) (2023) 965–972.

[84] J. Kim, S. Torquato, Theoretical prediction of the effective dynamic dielectric constant of disordered hyperuniform anisotropic composites beyond the long-wavelength regime, Opt. Mater. Express 14 (1) (2024) 194–215.

[85] G. Zhang, F.H. Stillinger, S. Torquato, Transport, geometrical and topological properties of stealthy disordered hyperuniform two-phase systems, J. Chem. Phys. 145 (2016) 244109.

[86] D. Chen, S. Torquato, Designing disordered hyperuniform two-phase materials with novel physical properties, Acta Mater. 142 (2018) 152–161.

[87] Y. Xu, S. Chen, P.-E. Chen, W. Xu, Y. Jiao, Microstructure and mechanical properties of hyperuniform heterogeneous materials, Phys. Rev. E 96 (2017) 043301.
[88] Y. Zheng, L. Liu, H. Nan, Z.-X. Shen, G. Zhang, D. Chen, L. He, W. Xu, M. Chen, Y. Jiao, H. Zhuang, Disordered hyperuniformity in two-dimensional amorphous silica, Sci. Adv. 6 (2020) eaba0826.
[89] O.H.E. Philcox, S. Torquato, Disordered heterogeneous universe: Galaxy distribution and clustering across length scales, Phys. Rev. X 13 (2023) 011038.
[90] M. Huang, W. Hu, S. Yang, Q.-X. Liu, H. Zhang, Circular swimming motility and disordered hyperuniform state in an algae system, Proc. Natl. Acad. Sci. 118 (18) (2021) e2100493118.
[91] Z. Ge, The hidden order of Turing patterns in arid and semi-arid vegetation ecosystems, Proc. Natl. Acad. Sci. 120 (42) (2023) e2306514120.
[92] M.A. Klatt, J. Lovrić, D. Chen, S.C. Kapfer, F.M. Schaller, P.W.A. Schönhöfer, B.S. Gardiner, A.-S. Smith, G.E. Schröder-Turk, S. Torquato, Universal hidden order in amorphous cellular geometries, Nat. Commun. 10 (2019) 811.
[93] J.W. Cahn, J.E. Hilliard, Free energy of a nonuniform system. I. Interfacial free energy, J. Chem. Phys. 28 (1958) 258–267.
[94] J.W. Cahn, Phase separation by spinodal decomposition in isotropic systems, J. Chem. Phys. 42 (1965) 93–99.
[95] P.M. Chaikin, T.C. Lubensky, Principles of Condensed Matter Physics, Cambridge University Press, New York, 1995.
[96] E. Hopf, Some topics of ergodic theory, in: L. Amerio, B. Segre (Eds.), Sistemi Dinamici E Teoremi Ergodici, Springer, Berlin, Heidelberg, 2011, pp. 47–112.
[97] R.S. Spencer, R.M. Wiley, The mixing of very viscous liquids, J. Colloid Sci. 6 (2) (1951) 133–145.
[98] J.M. Ottino, The Kinematics of Mixing: Stretching, Chaos, and Transport, Cambridge Univ. Press, Cambridge, U.K, 1989.
[99] S. Wiggins, J.M. Ottino, Foundations of chaotic mixing, Phil. Trans. R. Soc. A 362 (1818) (2004) 937–970, publisher: Royal Society.
[100] R. Sturman, J.M. Ottino, S. Wiggins, The Mathematical Foundations of Mixing: The Linked Twist Map As a Paradigm in Applications: Micro to Macro, Fluids to Solids, Cambridge Monographs on Applied and Computational Mathematics, Cambridge University Press, 2006.
[101] P.-E. Chen, R. Raghavan, Y. Zheng, H. Li, K. Ankit, Y. Jiao, Quantifying microstructural evolution via time-dependent reduced-dimension metrics based on hierarchical $n$-point polytope functions, Phys. Rev. E 105 (2022) 025306.
[102] P. Debye, H.R. Anderson, H. Brumberger, Scattering by an inhomogeneous solid, II. The correlation function and its applications, J. Appl. Phys. 28 (1957) 679–683.
[103] S. Torquato, F.H. Stillinger, New conjectural lower bounds on the optimal density of sphere packings, Experim. Math. 15 (2006) 307–331.
[104] S. Torquato, Disordered hyperuniform heterogeneous materials, J. Phys. Cond. Mat. 28 (2016) 414012.
[105] D.D. Battista, D. Ancora, G. Zacharakis, G. Ruocco, M. Leonetti, Hyperuniformity in amorphous speckle patterns, Opt. Express 26 (12) (2018) 15594–15608.
[106] E. Lomba, J.-J. Weis, L. Guisández, S. Torquato, Minimal statistical–mechanical model for multihyperuniform patterns in avian retina, Phys. Rev. E 102 (2020) 012134.
[107] S. Torquato, Structural characterization of many-particle systems on approach to hyperuniform states, Phys. Rev. E 103 (2021) 052126.
[108] H.E. Stanley, Introduction to Phase Transitions and Critical Phenomena, Oxford University Press, New York, 1987.
[109] J.J. Binney, N.J. Dowrick, A.J. Fisher, M.E.J. Newman, The Theory of Critical Phenomena: An Introduction to the Renormalization Group, Oxford University Press, Oxford, England, 1992.
[110] B.B. Mandelbrot, The Fractal Geometry of Nature, W. H. Freeman, New York, 1982.
[111] S. Torquato, J. Kim, M.A. Klatt, Local number fluctuations in hyperuniform and nonhyperuniform systems: Higher-order moments and distribution functions, Phys. Rev. X 11 (2021) 021028.
[112] E.C. Oğuz, J.E.S. Socolar, P.J. Steinhardt, S. Torquato, Hyperuniformity and anti-hyperuniformity in one-dimensional substitution tilings, Acta Cryst. Sect. A: Found. Adv. A 75 (2019) 3–13.
[113] S. Atkinson, G. Zhang, A.B. Hopkins, S. Torquato, Critical slowing down and hyperuniformity on approach to jamming, Phys. Rev. E 94 (2016) 012902.
[114] D. Chen, E. Lomba, S. Torquato, Binary mixtures of charged colloids: A potential route to synthesize disordered hyperuniform materials, Phys. Chem. Chem. Phys. 20 (2018) 17557–17562.
[115] D.P. Petersen, D. Middleton, Sampling and reconstruction of wave-number-limited functions in N-dimensional Euclidean spaces, Info. Control 5 (1962) 279–323.
[116] K. Rundman, J. Hilliard, Early stages of spinodal decomposition in an aluminum-zinc alloy, Acta Metall. 15 (6) (1967) 1025–1033.
[117] C.A. Smolders, J.J. van Aartsen, A. Steenbergen, Liquid-liquid phase separation in concentrated solutions of non-crystallizable polymers by spinodal decomposition, Kolloid-Z. Z. Polym. 243 (1) (1971) 14–20.
[118] A. Guell Izard, J. Bauer, C. Crook, V. Turlo, L. Valdevit, Ultrahigh energy absorption multifunctional spinodal nanoarchitectures, Small 15 (45) (2019) 1903834.
[119] M.-T. Hsieh, B. Endo, Y. Zhang, J. Bauer, L. Valdevit, The mechanical response of cellular materials with spinodal topologies, J. Mech. Phys. Solids 125 (2019) 401–419.
[120] C.M. Portela, A. Vidyasagar, S. Krödel, T. Weissenbach, D.W. Yee, J.R. Greer, D.M. Kochmann, Extreme mechanical resilience of self-assembled nanolabyrinthine materials, Proc. Natl. Acad. Sci. 117 (11) (2020) 5686–5693.
[121] S. Kumar, S. Tan, L. Zheng, D.M. Kochmann, Inverse-designed spinodoid metamaterials, Npj Comput. Mater. 6 (1) (2020) 1–10.
[122] F.V. Senhora, E.D. Sanders, G.H. Paulino, Optimally-tailored spinodal architected materials for multiscale design and manufacturing, Adv. Mater. 34 (26) (2022) 2109304.
[123] J.P. Hansen, I.R. McDonald, Theory of Simple Liquids, fourth ed., Academic Press, New York, 2013.
[124] N.F. Berk, Scattering properties of the leveled-wave model of random morphologies, Phys. Rev. A 44 (1991) 5069–5079.
[125] J.-S. Ferenc, Z. Néda, On the size distribution of Poisson voronoi cells, Physica A 385 (2) (2007) 518–526.
[126] J. Wuttke, Numerically stable form factor of any polygon and polyhedron, J. Appl. Crystallogr. 54 (2) (2021) 580–587.
[127] J. Kim, S. Torquato, Characterizing the hyperuniformity of ordered and disordered two-phase media, Phys. Rev. E 103 (2021) 012123.
[128] J. Kim, S. Torquato, Effect of imperfections on the hyperuniformity of many-body systems, Phys. Rev. B 97 (2018) 054105.
[129] M. Salvalaglio, M. Bouabdellaoui, M. Bollani, A. Benali, L. Favre, J.-B. Claude, J. Wenger, P. de Anna, F. Intonti, A. Voigt, M. Abbarchi, Hyperuniform monocrystalline structures by spinodal solid-state dewetting, Phys. Rev. Lett. 125 (2020) 126101.
[130] E.C. McGarrigle, K.T. Delaney, L. Balents, G.H. Fredrickson, Emergence of a spin microemulsion in spin–orbit coupled bose-einstein condensates, Phys. Rev. Lett. 131 (2023) 173403.
[131] C.J. Gommes, Small-angle scattering and scale-dependent heterogeneity, J. Appl. Crystallogr. 49 (4) (2016) 1162–1176.
[132] C.L.Y. Yeong, S. Torquato, Reconstructing random media, Phys. Rev. E 57 (1998) 495–506.